

# Convergence and Error Analysis of FE-HMM/FE<sup>2</sup> for Energetically Consistent Micro-Coupling Conditions in Linear Elastic Solids

Andreas Fischer, Bernhard Eidel\*

Heisenberg-Group, Institute of Mechanics, Department Mechanical Engineering  
University Siegen, 57068 Siegen, Paul-Bonatz-Str. 9-11, Germany

\*e-mail: bernhard.eidel@uni-siegen.de, phone: +49 271 740 2224, fax: +49 271 740 2436

## Abstract

A cornerstone of numerical homogenization is the equivalence of the microscopic and the macroscopic energy densities, which is referred to as Hill-Mandel condition. Among these coupling conditions, the cases of periodic, linear displacement and constant traction conditions are most prominent in engineering applications. While the stiffness hierarchy of these coupling conditions is a theoretically established and numerically verified result, very little is known about the numerical errors and convergence properties for each of them in various norms. The present work addresses these aspects both on the macroscale and the microscale for linear as well as quadratic finite element shape functions. The analysis addresses aspects of (i) regularity and how its loss affects the convergence behavior on both scales compared with the a priori estimates, of (ii) error propagation from micro to macro and of (iii) optimal micro-macro mesh refinement strategy. For constant traction conditions two different approaches are compared. The performance of a recovery-type error estimation based on superconvergence is assessed. All results of the present work are valid for both the Finite Element Heterogeneous Multiscale Method FE-HMM and for FE<sup>2</sup>.

**Keywords:** Computational homogenization; Macro-to-micro modeling; Convergence analysis; Error estimation; Finite element methods

## 1 Introduction

The overall aim of computational homogenization is to compute effective properties of microheterogeneous materials. This can be done in an a priori fashion in that effective properties are the result of pre-computations, which enables the identification of parameters in a constitutive law. In strongly nonlinear regimes as for inelastic material behavior, effective properties are rather calculated on the fly in direct micro-macro transitions. The first approach can be seen as a sequential or hierarchical multiscale method, the second variant as a concurrent multiscale method. In either case the methods aim at a trade-off of accuracy with efficiency by capturing the real microstructure along with a sampling of it in volumes of confined size. If the sampling regions are statistically representative, they are referred to as representative volume element (RVE). While an RVE is uncritical to identify for periodic microstructures, the proper choice of the RVE for non-periodic microstructures and random heterogeneous materials is still an item of ongoing research, see e.g. Ostoja-Starzewski [2006], Doskar et al. [2018] and references therein.

Among concurrent two-scale methods with direct micro macro transitions the so-called FE<sup>2</sup> has been advanced in different directions of non-linear solid mechanics and used in a

multitude of engineering applications, Michel et al. [1999], Miehe et al. [1999a], Miehe et al. [1999b], Fish et al. [1999], Feyel and Chaboche [2000], Kouznetsova et al. [2001], Kouznetsova et al. [2002], Kanit et al. [2003], Peric et al. [2010], Geers et al. [2010a], Geers et al. [2010b], Larsson et al. [2011], Schröder [2014], Saeb et al. [2016], Javili et al. [2017]. More recently, the FE<sup>2</sup> framework has been extended to transient computational homogenization Pham et al. [2013] and to the elastodynamics of metamaterials and of phononic crystals Sridhar et al. [2018].

In spite of these advancements, there is a remarkable lack of knowledge about the mathematical properties of FE<sup>2</sup> in a fully or semi-discrete setting as a two-scale finite element method. Here, the so-called Finite Element Heterogeneous Multiscale Method FE-HMM has made substantial contributions providing unified error estimates that comprise the macro error, the total micro error, and the modeling error Abdulle [2005], Abdulle and Schwab [2005], E et al. [2005], Ohlberger [2005], Abdulle [2009], Abdulle et al. [2012]. This advances the understanding and knowledge of FE-HMM, although the obtained results are currently restricted to linear problems; in solid mechanics to the purely linear setting of linear elastic material behavior along with geometrical linearity, Abdulle [2006], Jecker and Abdulle [2016]. Beyond the theoretical relevance of a priori error estimates they are of practical relevance, since they prescribe, how a uniform micro-macro refinement strategy shall be carried out in order to achieve optimal convergence for minimal computational efforts.

FE<sup>2</sup> and FE-HMM have been developed independently from each other and on almost parallel avenues without joint links or crossroads, FE<sup>2</sup> in mechanics, FE-HMM in mathematics as an off-spring of the very general Heterogeneous Multiscale Method HMM, E and Engquist [2003], E, Engquist, and Huang [2003]. Quite recently it was shown that despite minor differences in the numerical setup<sup>1</sup> the two methods are equivalent and, as a consequence, the a priori estimates of FE-HMM equally apply for FE<sup>2</sup>, Eidel and Fischer [2018].

A theoretical sound and commonly accepted link between the scales is Hill's postulate of energy equivalence between micro and macro energy densities, Hill [1963], Hill [1972]. It is applied in both FE<sup>2</sup> and FE-HMM, for the latter method without reference to Hill's work, E and Engquist [2003]. Several micro boundary conditions (BC) fulfill the postulate, among them (i) the linear displacement BC also referred to as kinematically uniform BC (KUBC) or Dirichlet BC (DBC), the (ii) constant traction BC (TBC), also called static uniform BC (SUBC) or Neumann BC, and (iii) the periodic BC (PBC). These three micro-coupling conditions, which are frequently called canonical in view of their practical relevance can be ordered according to their stiffness in that PBC has its lower bound by Neumann BC and its upper bound by Dirichlet BC.

The present work aims to advance the understanding of FE<sup>2</sup> and FE-HMM in their numerical characteristics. For that aim we address the following aspects for the particular case of linear elasticity in a geometrical linear frame, since this setting allows for the direct comparison with the a priori estimates of FE-HMM:

1. The numerical error and its convergence is analyzed for the following set of energetically consistent BCs, for (i) KUBC/Dirichlet, for (ii) PBC and for (iii)

---

<sup>1</sup>While the micro-macro stiffness transfer in FE<sup>2</sup> refers to the homogenized tangent moduli, FE-HMM refers to the microstiffness matrix along with a transfer operator.

SUBC/Neumann.

While the hierarchy of stiffnesses for conditions (i)–(iii) is a theoretically established result that was verified in numerous numerical simulations, Suquet [1987], Miehe [2003], Kanit et al. [2003], Peric et al. [2010], the convergence for the different coupling conditions is largely unexplored; an exception is Yue and E [2007] for the scalar-valued field problem of transport/conductivity. One of the guiding questions is whether there are significant differences in errors and convergence between the micro coupling conditions, and if so, whether they are generally valid similar to the mentioned stiffness hierarchy. Moreover the analysis compares the measured convergence orders against the nominal a priori estimates in different norms. In this context, a discrimination between micro error convergence on the microscale and on the macroscale is relevant, where the latter implies a micro-to-macro error propagation and a somewhat unusual convergence estimate. In either case the regularity of the boundary value problems both on the macro- and the microscale –and its loss due to singularities– is of importance.

Beyond the analysis of different coupling conditions, we compare two different numerical approaches for constant traction conditions; the approach based on a simple mass-type diagonal perturbation of the stiffness matrix introduced by Miehe and Koch [2002]<sup>2</sup> with the more recent approach of Javili et al. [2017].

2. Error estimation based on the Superconvergent Patch Recovery (SPR) and its validation by comparison with the exact error.

The true numerical error can be calculated quite accurately by comparison of the approximate solution with a reference solution on extremely fine grids. In engineering practice however, suchlike overkill solutions along with error calculation in a post-processing step are not feasible. For that reason error estimation provides an efficient way to analyze accuracy on-the-fly given that the error estimation is validated.

3. For the above analyses of error computation and estimation a set of benchmark problems is considered. They span the range from highly regular boundary value problems (BVP) up to singularity-dominated cases for both the macro as well as the microscale in  $n_{dim} = 2$ .

## 2 The finite element heterogeneous multiscale method FE-HMM in a nutshell

To put things into perspective and for ready reference this section outlines an FE-HMM formulation for linear elasticity cf. Eidel and Fischer [2018].

### 2.1 Model problem of linear elasticity

We consider a body  $\mathcal{B}$ , a bounded subset of  $\mathbb{R}^d$ ,  $n_{dim} = 2, 3$ , with boundary  $\partial\mathcal{B} = \partial\mathcal{B}_D \cup \partial\mathcal{B}_N$  where the Dirichlet boundary  $\partial\mathcal{B}_D$  and the Neumann boundary  $\partial\mathcal{B}_N$  are disjoint sets. The closure of the body  $\mathcal{B}$  is denoted by  $\bar{\mathcal{B}}$ . The body, which exhibits an

<sup>2</sup>similarly used at finite strains in Miehe [2003].

inhomogeneous microstructure, is subject to body forces  $\mathbf{f}$  and surface tractions  $\bar{\mathbf{t}}$  and in static equilibrium.

**2.1.1 The microproblem** The displacement  $\mathbf{u}^\epsilon = (u_1^\epsilon, \dots, u_{n_{dim}}^\epsilon)$  of the body is given by the solution of the system

$$\begin{aligned} -\sigma_{ij,j}^\epsilon &= f_i & \text{in } \mathcal{B} \\ u_i^\epsilon &= \bar{u}_i & \text{on } \partial\mathcal{B}_D \\ \sigma_{ij}^\epsilon n_j &= \bar{t}_i & \text{on } \partial\mathcal{B}_N \end{aligned} \quad (1)$$

The constitutive law is assumed to be linear elastic  $\sigma_{ij}^\epsilon = \mathbb{A}_{ijklm}^\epsilon \varepsilon_{lm}$  where  $\mathbb{A}_{ijklm}^\epsilon$  is the fourth order elasticity tensor and  $\varepsilon_{ij}$  the infinitesimal strain tensor with  $\varepsilon_{ij}(\mathbf{u}^\epsilon) = 1/2 (u_{i,j}^\epsilon + u_{j,i}^\epsilon)$  or more compact,  $\boldsymbol{\varepsilon}(\mathbf{u}^\epsilon) = \mathbf{L} \mathbf{u}^\epsilon$  with the linear differential operator  $\mathbf{L}$ . Superscript  $\epsilon$  throughout indicates the dependency of suchlike marked quantities on the heterogeneity of the elastic material.

In (1)<sub>3</sub>,  $\mathbf{n} = (n_1, \dots, n_{dim})$  is the unit outward normal to  $\partial\mathcal{B}$ .

Multiplying the strong form (1) by a test function  $\mathbf{v} \in \mathcal{V}$  and the application of the Green formula yield the variational form:

Find  $\mathbf{u}^\epsilon$  such that

$$B_\epsilon(\mathbf{u}^\epsilon, \mathbf{v}) \stackrel{\text{def}}{=} \int_{\mathcal{B}} \sigma^\epsilon(\mathbf{u}^\epsilon) : \boldsymbol{\varepsilon}(\mathbf{v}) dV = \int_{\mathcal{B}} \mathbf{f} \cdot \mathbf{v} dV + \int_{\partial\mathcal{B}_N} \bar{\mathbf{t}} \cdot \mathbf{v} dA \stackrel{\text{def}}{=} \mathbf{F}(\mathbf{v}), \quad (2)$$

which must hold for all  $\mathbf{v} \in \mathcal{V}$ , where  $\mathcal{V}$  is the space of admissible (virtual) displacements that fulfill homogeneous Dirichlet BC

$$\mathcal{V} = \{\mathbf{v}; \mathbf{v} \in H^1(\mathcal{B})^{n_{dim}}, \mathbf{v}|_{\partial\mathcal{B}_D} = \mathbf{0}\}. \quad (3)$$

**2.1.2 The macroproblem** The strong form of the macroscopic/homogenized boundary value problem (BVP) reads

$$\begin{aligned} -\sigma_{ij,j}^0 &= \langle f_i \rangle & \text{in } \mathcal{B} \\ u_i^0 &= \langle \bar{u}_i \rangle_\Gamma & \text{on } \partial\mathcal{B}_D \\ \sigma_{ij}^0 n_j &= \langle \bar{t}_i \rangle_\Gamma & \text{on } \partial\mathcal{B}_N \end{aligned} \quad (4)$$

for a derivation see Eidel and Fischer [2018]. The macroscopic displacement is denoted by  $u_i^0$  and  $\mathbb{A}^0$  is the homogenized elasticity tensor. In (4)<sub>1,3</sub>  $\sigma_{ij}^0$  is the macroscopic stress obtained by a volume average over the microdomain.

The values for the Dirichlet as well as Neumann BC in (4)<sub>2,3</sub> are obtained by surface averages of corresponding BC in (1)<sub>2,3</sub>, for details we refer to Eidel and Fischer [2018]. Similarly,  $\langle f_i \rangle$  is the volume average of body forces in (1)<sub>1</sub>.

The solution of the homogenized problem is obtained from the variational form

$$B_0(\mathbf{u}^0, \mathbf{v}) = \int_{\mathcal{B}} \boldsymbol{\sigma}^0(\mathbf{u}^0) : \boldsymbol{\varepsilon}(\mathbf{v}) dV = \int_{\mathcal{B}} \mathbf{f} \cdot \mathbf{v} dV + \int_{\partial\mathcal{B}_N} \bar{\mathbf{t}} \cdot \mathbf{v} dA \quad \forall \mathbf{v} \in \mathcal{V}, \quad (5)$$

which follows from multiplying the strong form (4) by test functions  $\mathbf{v}$  along with the application of Green's formula. For notational convenience we skip in (5) and in the rest of the paper the averaging symbols  $\langle \bullet \rangle$ ,  $\langle \bullet \rangle_\Gamma$  for  $\mathbf{f}$ ,  $\bar{\mathbf{u}}$  and  $\bar{\mathbf{t}}$  but keep in mind that these quantities follow from volume and surface averages, respectively.

We consider the piecewise linear continuous FEM in macro- and microspace, respectively.

We define a macro finite element space as

$$\mathcal{S}_{\partial\mathcal{B}_D}^p(\mathcal{B}, \mathcal{T}_H) = \{ \mathbf{u}^H \in H^1(\mathcal{B})^d; \mathbf{u}^H|_{\partial\mathcal{B}_D} = \bar{\mathbf{u}}; \mathbf{u}^H|_K \in \mathcal{P}^p(K)^{n_{dim}}, \forall K \in \mathcal{T}_H \}, \quad (6)$$

where  $\mathcal{P}^p$  is the space of (here: linear,  $p = 1$ , or quadratic,  $p = 2$ ) polynomials on the element  $K$ ,  $\mathcal{T}_H$  the (quasi-uniform) triangulation of  $\mathcal{B} \subset \mathbb{R}^{n_{dim}}$ . Superscript  $H$  denotes the characteristic element size, with  $H \gg \epsilon$  for efficiency. The space  $\mathcal{S}_{\partial\mathcal{B}_D}^p$  is a subspace of  $\mathcal{V}$  defined in (3).

For the solution of (1) in the macrodomain we use the two-scale FEM framework of the FE-HMM as originally proposed in E and Engquist [2003] and analyzed for elliptic PDEs in E et al. [2005], and, with the focus on linear elasticity, in Abdulle [2006].

The macrosolution of the FE-HMM is given by the following variational form:

Find  $\mathbf{u}^H \in \mathcal{S}_{\partial\mathcal{B}_D}(\mathcal{B}, \mathcal{T}_H)$  such that

$$B_H(\mathbf{u}^H, \mathbf{v}^H) = \int_{\mathcal{B}} \mathbf{f} \cdot \mathbf{v}^H dV + \int_{\partial\mathcal{B}_N} \bar{\mathbf{t}} \cdot \mathbf{v}^H dA \quad \forall \mathbf{v}^H \in \mathcal{S}_{\partial\mathcal{B}_D}(\mathcal{B}, \mathcal{T}_H), \quad (7)$$

which reads as a standard finite element formulation.

## 2.2 The modified macro bilinear form of FE-HMM

If the homogenized constitutive tensor  $\mathbb{A}^0(\mathbf{x})$  is explicitly known, the bilinear form  $B_H(\mathbf{u}^H, \mathbf{v}^H)$  can be calculated using standard numerical quadrature according to (8), where  $\mathbf{x}_{K_l}$  and  $\omega_{K_l}$  are the quadrature points and quadrature weights, respectively

$$B_H(\mathbf{u}^H, \mathbf{v}^H) = \sum_{K \in \mathcal{T}_H} \sum_{l=1}^{N_{qp}} \omega_{K_l} [\boldsymbol{\sigma}^0(\mathbf{u}^H(\mathbf{x}_{K_l})) : \boldsymbol{\varepsilon}(\mathbf{v}^H(\mathbf{x}_{K_l}))] \quad (8)$$

$$\approx \sum_{K \in \mathcal{T}_H} \sum_{l=1}^{N_{qp}} \omega_{K_l} \left[ \frac{1}{|K_l|} \int_{K_l} \boldsymbol{\sigma}^\epsilon(\mathbf{u}_{K_l}^h) : \boldsymbol{\varepsilon}(\mathbf{v}_{K_l}^h) dV \right]. \quad (9)$$

Since  $\mathbb{A}^0(\mathbf{x})$  is typically not known for heterogeneous materials, the ansatz of FE-HMM is to approximate the virtual work expression at point  $\mathbf{x}_{K_l}$  in the semidiscrete form (8) by another bilinear form using the known microheterogeneous elasticity tensor  $\mathbb{A}^\epsilon$ , see (9). According to this approximation, the solution  $\mathbf{u}_{K_l}^h$  is obtained on microsampling domains  $K_{\delta_l} = \mathbf{x}_{K_l} + \delta [-1/2, +1/2]^{n_{dim}}$ ,  $\delta \geq \epsilon$ , which are each centered at the quadrature points  $\mathbf{x}_{K_l}$  of  $K$ ,  $l = 1, \dots, N_{qp}$ . For a visualization see Fig. 1. These microsampling domains with volume  $|K_{\delta_l}|$  provide the additive contribution to the stiffness matrix of the macro finite element. In order to avoid too heavy notation we will replace  $K_{\delta_l}$  by  $K_l$ .

The approximation of (8) by (9) indicates that FE-HMM crucially relies on a modified quadrature rule and fulfills the equality of the macroenergy density with the microenergy density, thus in agreement with Hill's postulate, Hill [1963], Hill [1972].

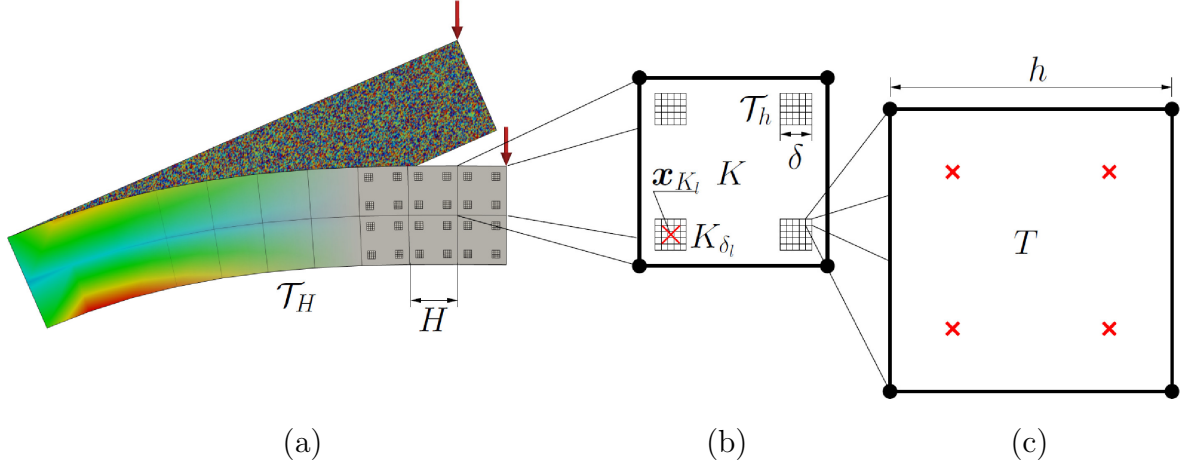


**Figure 1:** FE-HMM as a two-scale finite element method: (a) Macroscopic BVP with macro-triangulation  $\mathcal{T}_H$ , (b) one macro finite element  $K$  of size  $H$  with microdomains/RVEs  $K_{\delta_l}$  of triangulation  $\mathcal{T}_h$ , centered at the macro quadrature points  $\mathbf{x}_{K_l}$ , (c) micro finite element  $T$  of size  $h$  with standard quadrature points.

### 2.3 Variational formulation of the microproblem

It can be shown that the FE-HMM microproblem resembles the discrete version of the cell problem of asymptotic expansion, if it is formulated for each microdomain  $K_l$  in  $K$  with  $l = 1, \dots, N_{qp}$ ,  $K \in \mathcal{T}_H$  like this:

Find  $\mathbf{u}_{K_l}^h$  such that the conditions for macro-micro coupling and for the micro bilinear form (10) are fulfilled:

$$\left. \begin{aligned} (\mathbf{u}_{K_l}^h - \mathbf{u}_{lin, K_l}^H) &\in \mathcal{S}^q(K_l, \mathcal{T}_h) \\ B_{K_l}(\mathbf{u}_{K_l}^h, \mathbf{w}_{K_l}^h) &:= \int_{K_l} \boldsymbol{\sigma}^\varepsilon(\mathbf{u}_{K_l}^h) : \boldsymbol{\varepsilon}(\mathbf{w}_{K_l}^h) dV = 0 \\ \forall \mathbf{w}_{K_l}^h &\in \mathcal{S}^q(K_l, \mathcal{T}_h), \end{aligned} \right\} \quad (10)$$

where the micro finite element space  $\mathcal{S}^q(K_l, \mathcal{T}_h)$  is defined by

$$\mathcal{S}^q(K_l, \mathcal{T}_h) = \{\mathbf{w}^h \in \mathcal{W}(K_l); \mathbf{w}^h \in (\mathcal{P}^q(T))^{n_{dim}}, T \in \mathcal{T}_h\}. \quad (11)$$

In (11)  $\mathcal{T}_h$  is a quasi-uniform discretization of the sampling domain  $K_l$  with mesh size  $h \ll \varepsilon$  resolving the finescale and  $\mathcal{P}^q$  is the space of polynomials on the element  $T$ . In the present work we consider linear and quadratic shape functions,  $q = 1, 2$ . The particular choice of the Sobolev space  $\mathcal{W}(K_l)$  sets the boundary conditions for the micro problems, cf. Abdulle [2009], Sec. 3.2. Among the coupling conditions that fulfill Hill's postulate we consider (i) periodic BC (PBCs), (ii) kinematically uniform displacement conditions (KUBC), and (iii) constant traction conditions (TBC).

The linearization of  $\mathbf{u}^H$  in (10)<sub>1</sub> is carried out at the quadrature point  $\mathbf{x}_{K_l}$

$$\mathbf{u}_{lin, K_l}^H = \mathbf{u}^H(\mathbf{x}_{K_l}) + (\mathbf{x} - \mathbf{x}_{K_l}) \cdot \nabla \mathbf{u}^H(\mathbf{x}_{K_l}). \quad (12)$$

It ensures a homogeneous deformation on the microdomain and resembles therein the unit cell problem of asymptotic homogenization (the FE-HMM perspective) and thus is in the frame of strain-driven first order computational homogenization.

For the solution of (10) a basis  $\{N_I^H\}_{I=1}^{M_{mac}}$  for the macro finite element space  $\mathcal{S}_0^p(\mathcal{B}, \mathcal{T}_H)$  is employed in order to represent the macrosolution  $\mathbf{u}^H$  of (7). Similarly, a basis  $\{N_i^h\}_{i=1}^{M_{mic}}$  of the micro finite element space  $\mathcal{S}_0^q(K_l, \mathcal{T}_h)$ , (11), is introduced in order to represent the solution  $\mathbf{u}^h$  of a microproblem.  $M_{mac}$  denotes the number of nodes of the macrodomain, and  $M_{mic}$  denotes the number of nodes of each microdomain. Hence, the macro- and the microsolution follow the representation

$$\mathbf{u}^H = \sum_{I=1}^{M_{mac}} N_I^H \mathbf{d}_I^H, \quad \mathbf{u}^h = \sum_{i=1}^{M_{mic}} N_i^h \mathbf{d}_i^h, \quad (13)$$

where  $\mathbf{d}_I^H$  is the displacement vector of macronode  $I$ , and  $\mathbf{d}_i^h$  is the displacement vector for micronode  $i$ .

## 2.4 Macrostiffness calculation

The macro bilinear form  $B_H^e(\mathbf{u}^H, \mathbf{v}^H)$  is the virtual internal work for a macro finite element. The corresponding bilinear form in terms of the shape functions  $B_H^e(\mathbf{N}_I^H, \mathbf{N}_J^H)$  results in the macro element stiffness matrix contribution  $\mathbf{k}_{IJ}^{e,mac}$  for macronodes  $I, J$ , a  $d \times d$  matrix. It holds

$$\mathbf{k}_{IJ}^{e,mac} = B_H^e(\mathbf{N}_I^H, \mathbf{N}_J^H) = \sum_{l=1}^{N_{qp}} \frac{\omega_{K_l}}{|K_l|} \int_{K_l} (\mathbf{L}\mathbf{u}_{K_l}^{h(I)})^T \mathbb{A}^\epsilon(\mathbf{x}) \mathbf{L}\mathbf{u}_{K_l}^{h(J)} dV. \quad (14)$$

In (14)  $\mathbf{u}_{K_l}^{h(I)}$  is the counterpart of  $\mathbf{u}_{K_l}^h$  in (10). It is the dimensionless solution of the microproblem on  $K_l$ , which is driven by the shape function  $N_I^H$  at macronode  $I$ . In the following, we add  $x_i, i = 1, \dots, n_{dim}$  to account for the vector-valued field problem of dimension  $n_{dim}$ . Consequently,  $\mathbf{u}_{K_l}^{h(I, x_i)}$  is the microsolution driven by a macroelement unit-displacement state  $\mathbf{u}_{lin, K_l}^{H(I, x_i)}$  at node  $I$  in  $x_i$ -direction.

For stiffness calculation, problem (10) is reformulated in that  $\mathbf{u}_{K_l}^{h(I, x_i)}$  replaces  $\mathbf{u}_{K_l}^h$ .

For the coupling of  $\mathbf{u}_{lin, K_l}^{H(I, x_i)}$  with  $\mathbf{u}_{K_l}^{h(I, x_i)}$  the two fields are expanded into the same basis  $\{N_i^h\}_{i=1}^{M_{mic}}$  of  $\mathcal{S}^q(K_l, \mathcal{T}_h)$ ,

$$\mathbf{u}_{lin, K_l}^{H(I, x_i)} = \sum_{m=1}^{M_{mic}} N_{m, K_l}^h \mathbf{d}_m^{H(I, x_i)}, \quad \mathbf{u}_{K_l}^{h(I, x_i)} = \sum_{m=1}^{M_{mic}} N_{m, K_l}^h \mathbf{d}_m^{h(I, x_i)}. \quad (15)$$

The solution of the microproblems for the minimizers  $\mathbf{d}^{h(I, x_i)}$  is presented in Sec. 2.5. The macroelement stiffness matrix according to (14) yields after some algebra

$$\begin{aligned} \mathbf{k}_{IJ}^{e,mac} &= B_H^e[\mathbf{N}_I^H, \mathbf{N}_J^H] \\ &= \sum_{l=1}^{N_{qp}} \frac{\omega_{K_l}}{|K_l|} (\mathbf{d}^{h(I)})^T \mathbf{K}_{K_l}^{mic} \mathbf{d}^{h(J)}, \end{aligned} \quad (16)$$

where  $\mathbf{d}^{h(I)} = (\mathbf{d}^{h(I, x_1)} | \mathbf{d}^{h(I, x_2)} | \mathbf{d}^{h(I, x_3)})$  for  $n_{dim} = 3$ . A detailed derivation of (16) is presented in the appendix, Sec. A.

The assembly of  $\mathbf{k}_{IJ}^{e,mac}$  results in  $\mathbf{k}^{e,mac}$  and implies a column-wise assembly of  $\mathbf{d}^{h(I)}$  for  $I = 1, \dots, N_{node}$  that results in the transformation matrix  $\mathbf{T}_{K_l}$

$$\mathbf{k}_K^{e,mac} = \sum_{l=1}^{N_{qp}} \frac{\omega_{K_l}}{|K_l|} \mathbf{T}_{K_l}^T \mathbf{K}_{K_l}^{mic} \mathbf{T}_{K_l} \quad (17)$$

$$\text{with } \mathbf{T}_{K_l} = \left[ \left[ \mathbf{d}^{h(I,x_i)} \right]_{i=1,\dots,n_{dim}} \right]_{I=1,\dots,N_{node}}. \quad (18)$$

The matrix dimensions

$$\begin{aligned} \mathbf{T}_{K_l}^T &\in \mathbb{R}^{(N_{node} \cdot n_{dim}) \times (M_{mic} \cdot n_{dim})}, & \mathbf{K}_{K_l}^{mic} &\in \mathbb{R}^{(M_{mic} \cdot n_{dim}) \times (M_{mic} \cdot n_{dim})}, & \mathbf{T}_{K_l} &\in \mathbb{R}^{(M_{mic} \cdot n_{dim}) \times (N_{node} \cdot n_{dim})} \\ \mathbf{k}_K^{e,mac} &\in \mathbb{R}^{(N_{node} \cdot n_{dim}) \times (N_{node} \cdot n_{dim})} \end{aligned}$$

underpin that  $\mathbf{T}_{K_l}$  is not only the agency of a micro-to-macro stiffness transfer but also a compression operator that transforms  $\mathbf{K}_K^{mic}$  into  $\mathbf{k}_K^{e,mac}$ .

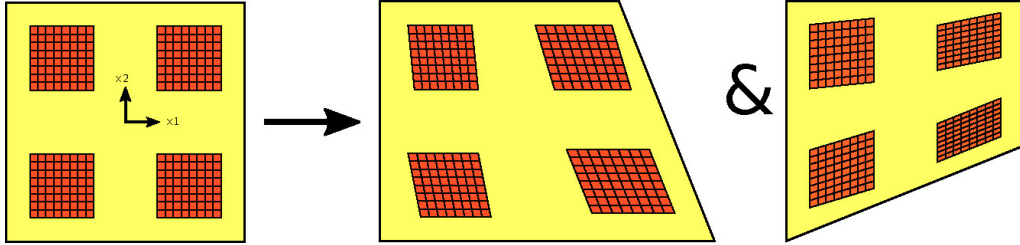


**Figure 2:** Unit displacement states in  $x_i$ -directions,  $i = 1, 2$  applied to the lower right macro element node  $I$  and the uniform deformations of the microdomains/RVEs.

In the context of stiffness computation, a macro element shape function represents a unit displacement state for macro node  $I$ ,  $I = 1, \dots, N_{node}$  in each direction of space  $x_i \mid i = 1, \dots, n_{dim}$ . They drive the microproblem in terms of the corresponding nodal values  $\mathbf{d}_m^{H(I,x_i)}$ ,  $m = 1, \dots, M_{mic}$  in each microdomain to evaluate the macroelement stiffness  $\mathbf{k}_{IJ}^{e,mac}$ . Each unit displacement state in  $x_i$ -direction induces in  $\mathbf{d}^{H(I,x_i)}$  nonzero components only in  $x_i$ , for example  $\mathbf{d}^{H(I,x_i)}|_{i=2} = \left[ 0, d_{1,x_2}^{H(I,x_2)}, 0, \dots, 0, d_{M_{mic},x_2}^{H(I,x_2)}, 0 \right]^T$ .

Figure 2 visualizes two unit displacement states applied to the lower right macronode in two directions along with the corresponding uniform RVE-deformations that follow from linearization according to (12).

## 2.5 Solution of the microproblems

The microstiffness matrix is obtained by Gauss-Legendre numerical quadrature on the element level, the assembly of the element stiffness matrices results in the total stiffness matrix for an RVE.

With the RVE microstiffness matrix in hand, the microproblem can be solved. Here the method of Lagrange multipliers is chosen such that a saddlepoint problem must be solved. The total energy for a macro unit displacement state reads

$$\begin{aligned} \mathcal{L}(\mathbf{d}^{h(I,x_i)}, \boldsymbol{\lambda}^{(I,x_i)}) &= \frac{1}{2} (\mathbf{d}^{h(I,x_i)})^T \mathbf{K}_{K_l}^{mic} \mathbf{d}^{h(I,x_i)} + \boldsymbol{\lambda}^{(I,x_i)T} \mathbf{G} \left( \mathbf{d}^{h(I,x_i)} - \bar{\mathbf{d}}^{H(I,x_i)} \right) \quad (19) \\ &\text{for } I = 1, \dots, N_{node}, \text{ and } x_i \mid i = 1, \dots, n_{dim}, \end{aligned}$$

where  $\mathbf{G}$  contains the kinematical coupling constraints. Details of various coupling conditions and their implementation in the frame of Lagrange multipliers are described in Sec. 3. In either case the Lagrange multipliers represent external forces which enforce the micro coupling condition.

The vector of Lagrange multipliers  $\boldsymbol{\lambda}^{(I,x_i)} \in \mathbb{R}^{(1+L) \cdot n_{dim}}$ , where  $L$  depends on the type of microcoupling, reads for  $n_{dim} = 3$  as

$$\boldsymbol{\lambda}^{(I,x_i)} = \{\lambda_{0,x_1}^{(I,x_i)}, \lambda_{0,x_2}^{(I,x_i)}, \lambda_{0,x_3}^{(I,x_i)}, \lambda_{1,x_1}^{(I,x_i)}, \lambda_{1,x_2}^{(I,x_i)}, \lambda_{1,x_3}^{(I,x_i)}, \dots, \lambda_{L,x_1}^{(I,x_i)}, \lambda_{L,x_2}^{(I,x_i)}, \lambda_{L,x_3}^{(I,x_i)}\}^T. \quad (20)$$

The first variation of  $\mathcal{L}$  with respect to  $\mathbf{d}^{h(I,x_i)}$  and  $\boldsymbol{\lambda}^{(I,x_i)}$  results in the stationarity conditions

$$\begin{bmatrix} \mathbf{K}_{K_l}^{mic} & \mathbf{G}^T \\ \mathbf{G} & \mathbf{0} \end{bmatrix} \begin{bmatrix} \mathbf{d}^{h(I,x_i)} \\ \boldsymbol{\lambda}^{(I,x_i)} \end{bmatrix} = \begin{bmatrix} \mathbf{0} \\ \mathbf{G} \mathbf{d}^{H(I,x_i)} \end{bmatrix} \text{ for } I = 1, \dots, N_{node}, \quad i = 1, \dots, n_{dim}. \quad (21)$$

The solution of (21) subject to  $N_{node} \cdot n_{dim}$  right hand sides can be carried out efficiently since the coefficient matrix in (21) is constant. The solution vectors are augmented to full matrices, hence,  $\mathbf{d}^{h(I,x_i)} \rightarrow \mathbf{T}$ ,  $\boldsymbol{\lambda}^{(I,x_i)} \rightarrow \boldsymbol{\Lambda}$ ,  $\mathbf{d}^{H(I,x_i)} \rightarrow \mathbf{d}^H$ .

The solution of (21) serves the purpose to compute the transformation matrix  $\mathbf{T}_{K_l}$  according to (18). After the consecutive solution of the global macroproblem for  $\mathbf{u}^H$ , the microproblems have to be solved. Then, (21) is driven by the true macroscopic displacement vector  $\mathbf{d}^H$ , which results in the true microdisplacements  $\mathbf{d}^h$ .

### 3 The coupling conditions

This section gives a brief account of the implementation of the coupling conditions (Dirichlet, periodic and Neumann) in a Lagrange-Multiplier framework. Doing so, the particular format of the constraint matrix  $\mathbf{G}$  is detailed.

#### 3.1 Dirichlet coupling

The simplest coupling condition is the Dirichlet coupling, where linear displacements following from the macro displacement field are applied to the boundaries of a microdomain

$$\mathbf{u}_{K_l}^{h(I,x_i)} = \mathbf{u}_{lin,K_l}^{H(I,x_i)} \quad \text{on } \partial K_l. \quad (22)$$

In this case the constraint matrix  $\mathbf{G}$  contains  $L \cdot n_{dim}$  rows with  $L$  the number of boundary nodes and  $n_{dim}$  the number of degrees of freedom per node. Each row contains a 1 pointing at a degree of freedom of a boundary node and 0 elsewhere. By doing so (21) directly couples the nodal micro displacements  $\mathbf{d}^{h(I,x_i)}$  on the RVE boundary to the nodal micro displacements following from the macro displacement field  $\mathbf{d}^{H(I,x_i)}$ .

The expression on the right hand side of the system of equations  $\mathbf{G} \mathbf{d}^{H(I,x_i)}$  can be derived by inserting the micro coordinates of the boundary nodes in the reference configuration into the linearized macro shape functions.

### 3.2 Periodic coupling

Periodic coupling conditions imply periodic displacements and anti-periodic tractions on the boundaries of the microdomain. It holds

$$\left( \mathbf{u}_{K_l}^{h(I,x_i)} - \mathbf{u}_{lin,K_l}^{H(I,x_i)} \right)^+ = \left( \mathbf{u}_{K_l}^{h(I,x_i)} - \mathbf{u}_{lin,K_l}^{H(I,x_i)} \right)^- \quad (23)$$

$$\mathbf{t}^+ = -\mathbf{t}^-. \quad (24)$$

The boundary of the microdomain is here split up in a part  $\partial K_l^+$  and a part  $\partial K_l^-$  such that  $\partial K_l^+ \cup \partial K_l^- = \partial K_l$  having opposite outward normal vectors  $\mathbf{n}^+ = -\mathbf{n}^-$ .

The constraint matrix  $\mathbf{G}$  then contains  $L \cdot n_{dim}$  rows with  $L$  the number of non-redundant periodic couples and  $n_{dim}$  the number of degrees of freedom per node. The single rows of the constraint matrix contain a 1 pointing at a degree of freedom of a node on  $\partial K_l^+$  and a -1 pointing at the corresponding degree of freedom of the node on  $\partial K_l^-$ , the other entries of  $\mathbf{G}$  vanish.

Periodic displacement fluctuations only eliminate the rotational rigid body motions, the rigid body translations however are not discarded by PBC. For that reason they must be eliminated by an additional condition

$$\int_{K_l} \left( \mathbf{u}_{K_l}^{h(I,x_i)} - \mathbf{u}_{lin,K_l}^{H(I,x_i)} \right) dV = \mathbf{c}. \quad (25)$$

Since (25) is a normalization condition for the periodic fluctuations, the particular choice of the constant is inconsequential for the microsolution. Here we choose  $\mathbf{c} = \mathbf{0}$ .

By multiplying the transpose of  $\mathbf{G}$  with the Lagrange multipliers, the anti-periodic tractions for each couple of periodic nodes are realized.

For  $n_{dim} = 3$  matrix  $\mathbf{G}$  exhibits the format

$$\mathbf{G} = \begin{bmatrix} b_1 & 0 & 0 & \dots & b_{M_{mic}} & 0 & 0 \\ 0 & b_1 & 0 & \dots & 0 & b_{M_{mic}} & 0 \\ 0 & 0 & b_1 & \dots & 0 & 0 & b_{M_{mic}} \\ & & & \overline{\mathbf{G}} & & & \end{bmatrix}. \quad (26)$$

In  $\mathbf{G}$ , the first  $d$  rows contain the normalization condition for the fluctuations, to which the first  $d$  Lagrange multipliers are associated. The coefficients  $b_i$ ,  $i = 1, \dots, M_{mic}$  in (26) follow from the coupling condition (25). It holds

$$\int_{K_\delta} \mathbf{u}^{h(I,x_i)} dV = \sum_{T \in \mathcal{T}_h} \sum_{m=1}^{M_{mic}} \mathbf{d}_m^{h(I,x_i)} \underbrace{\int_T \mathbf{N}_m^h dV}_{=: b_m} = \sum_{T \in \mathcal{T}_h} \mathbf{d}^{h(I,x_i)} \cdot \mathbf{b} \quad (27)$$

$$\int_{K_\delta} \mathbf{u}_{lin}^{H(I,x_i)} dV = \sum_{T \in \mathcal{T}_h} \sum_{m=1}^{M_{mic}} \mathbf{d}_m^{H(I,x_i)} \int_T \mathbf{N}_m^h dV = \sum_{T \in \mathcal{T}_h} \mathbf{d}^{H(I,x_i)} \cdot \mathbf{b} \quad (28)$$

$$\text{where } b_m = \int_T \mathbf{N}_m^h dV. \quad (29)$$

### 3.3 Neumann coupling

The Neumann coupling condition of constant tractions on the element boundary reads as

$$\mathbf{t}(\mathbf{x}) = \boldsymbol{\sigma}_{K_l}(\mathbf{u}^{H(I,x_i)}) \mathbf{n}(\mathbf{x}) \quad \text{on } \partial K_l. \quad (30)$$

Since stress of the macro Gauss point  $\boldsymbol{\sigma}_{K_l}(\mathbf{u}^{H(I,x_i)})$  for macro unit displacement states is not known, the condition is reformulated to a weak constraint in terms of a macroscopic strain  $\boldsymbol{\varepsilon}_{K_l}(\mathbf{u}^{H(I,x_i)})$  cf. Miehe and Koch [2002]

$$\frac{1}{|K_l|} \int_{\partial K_l} \text{sym}[\mathbf{u}^{h(I,x_i)}(\mathbf{x}) \otimes \mathbf{n}] dA = \boldsymbol{\varepsilon}_{K_l}(\mathbf{u}^{H(I,x_i)}). \quad (31)$$

Introducing a discrete nodal normal vector

$$\mathbf{n}_q := \frac{1}{2}[\mathbf{x}_{q+1} - \mathbf{x}_{q-1}] \times \mathbf{e}_3 \quad (32)$$

with  $\mathbf{x}_{q-1}$  and  $\mathbf{x}_{q+1}$  being the neighbor nodes of node  $q$  on the boundary, we get

$$\frac{1}{|K_l|} \sum_{q=1}^L \text{sym}[\mathbf{d}_q^{h(I,x_i)} \otimes \mathbf{n}_q] = \boldsymbol{\varepsilon}_{K_l}(\mathbf{u}^{H(I,x_i)}), \quad (33)$$

where  $L$  is the number of nodes on the boundary of the microdomain. The neighboring nodes  $\mathbf{x}_{q-1}$  and  $\mathbf{x}_{q+1}$  have to be oriented so that  $\mathbf{n}_q$  is an outward normal vector.

Expression (33) can be recast into a matrix representation

$$\sum_{q=1}^M \mathbf{G}_q \mathbf{d}_q^{h(I,x_i)} = \boldsymbol{\varepsilon}_{K_l}(\mathbf{u}^{H(I,x_i)}), \quad (34)$$

where  $\mathbf{G}_q$  is depending on the normal vector  $\mathbf{n}_q$  and reads as

$$\mathbf{G}_q := \frac{1}{|K_l|} \begin{bmatrix} 2n_1 & 0 \\ 0 & 2n_2 \\ n_2 & n_1 \end{bmatrix}_q, \quad (35)$$

for  $n_{dim} = 2$ . The constraint matrix  $\mathbf{G}$  follows from assembling the single  $\mathbf{G}_q$  matrices

$$\mathbf{G} \mathbf{d}^{h(I,x_i)} = \boldsymbol{\varepsilon}_{K_l}(\mathbf{u}^{H(I,x_i)}) \quad \text{on } \partial K_l. \quad (36)$$

The term on the right hand side of (21) can also be replaced by the strains  $\boldsymbol{\varepsilon}_{K_l}(\mathbf{u}^{H(I,x_i)})$ .

Again, the constant traction BC alone does not eliminate the rigid body motions of the RVE and the corresponding zero eigenvalues of the stiffness matrix. The rigid body motions must be eliminated by additional kinematical constraints (3 for  $n_{dim} = 2$  and 6 for  $n_{dim} = 3$ ), which can be realized e.g. by a so-called semi-Dirichlet coupling introduced in Javili et al. [2017].

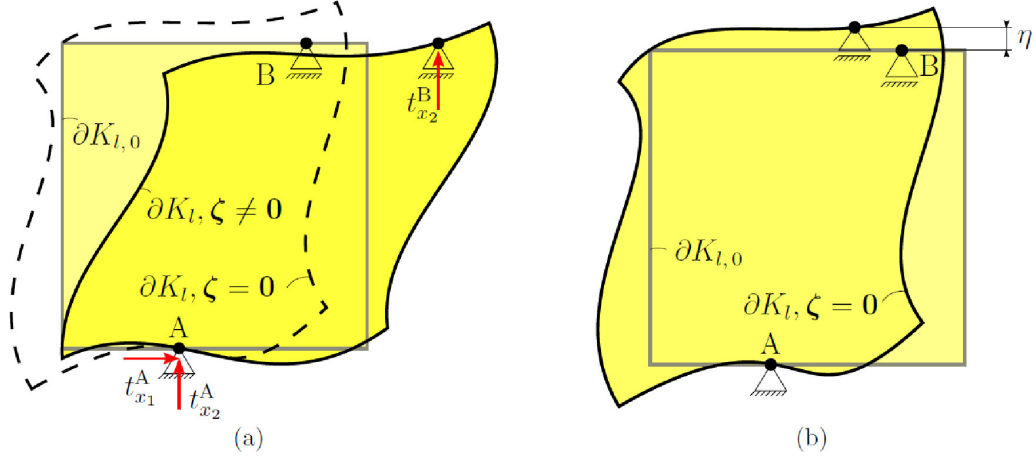


**Figure 3: Semi-Dirichlet BC for Neumann coupling:**(a) Elimination of rigid body motions in  $n_{dim} = 2$  by adding three Dirichlet BC at single nodes, which renders the system statically determined. Undeformed microdomain  $\partial K_{l,0}$  fixed at node A and node B and deformed microdomain  $\partial K_l$  with and without the additional displacement constraints, (b) variation of  $\eta$  to realize the constant traction condition without spurious forces in A and B.

In Fig. 3 (a) the additional Dirichlet BC in points A and B and their influence on the reaction forces on the boundary are shown. The reaction forces in A and B can be given in terms of the stress  $\sigma_{K_l}$  in the corresponding macro quadrature point

$$\mathbf{t}^A = \sigma_{K_l} \cdot \mathbf{n}^A + \boldsymbol{\zeta}^A, \quad (37)$$

$$\mathbf{t}^B = \sigma_{K_l} \cdot \mathbf{n}^B + \boldsymbol{\zeta}^B. \quad (38)$$

To enforce the Dirichlet BC in A and B, an additional force is needed which influences the reaction forces in A and B. In order to satisfy (30), the Dirichlet BC have to be chosen such that  $\boldsymbol{\zeta}^A = \boldsymbol{\zeta}^B = \mathbf{0}$ .

To do so the Dirichlet condition in point B, where (here) the node is merely fixed in  $x_2$  direction, is modified by moving point B from its former position about  $\eta$  in  $x_2$  direction. This has to be done until (36) and  $\boldsymbol{\zeta}^A = \boldsymbol{\zeta}^B = \mathbf{0}$  are satisfied. Writing down these conditions in a residual vector  $\mathbf{R}$  leads to

$$\mathbf{R}(\sigma_{K_l}, \eta) = \left[ \mathbf{G}d^{h(I,x_i)} - \boldsymbol{\varepsilon}_{K_l}^{(I,x_i)}, \boldsymbol{\zeta}^{(B(I,x_i))} \right] \stackrel{!}{=} \mathbf{0}, \quad (39)$$

which is solved using the Newton-Raphson scheme. Therefore (39) has to be linearized which results in

$$\mathbf{R}(\sigma_{K_l, i+1}, \eta_{i+1}) = \mathbf{R}(\sigma_{K_l, i}, \eta_i) + \frac{\partial \mathbf{R}}{\partial \sigma_{K_l}} \Big|_i : \Delta \sigma_{K_l, i} + \frac{\partial \mathbf{R}}{\partial \eta} \Big|_i \Delta \eta_i \stackrel{!}{=} \mathbf{0}. \quad (40)$$

The Lagrange multipliers which follow from the Neumann coupling condition contain the macroscopic stresses in the corresponding quadrature point. The Lagrange multipliers which follow from the semi-Dirichlet coupling contain the additional forces required to enforce the semi-Dirichlet constraints, which must vanish.

In contrast to the iterative, hence expensive solution using the semi-Dirichlet coupling where the micro system of equations has to be solved at least twice, the approach of Miehe and Koch [2002] enforces regularity of the microproblem by adding a perturbation to the entries on the diagonal of the micro stiffness matrix. Section 5 will provide a quantitative comparison of the methods.

### 3.4 Numerical implications of different coupling conditions

The above described coupling conditions all lead to the same system of equations (21) which has to be solved for the micro displacements. The numerical effort depends on the size of the system of equations and, in the case of Neumann coupling with semi-Dirichlet coupling, additionally on the number of required iterations.

While the micro stiffness matrix  $\mathbf{K}_{K_l}^{mic}$  exhibits the same format for all of the described coupling conditions, the constraints matrix  $\mathbf{G}$  does not. For Dirichlet coupling  $\mathbf{G}$  has  $L \cdot n_{dim}$  rows with  $L$  the number of boundary nodes and  $n_{dim}$  the number of degrees of freedom per node. In case of periodic coupling  $\mathbf{G}$  has  $L \cdot n_{dim}$  rows with  $L$  the number of non-redundant periodic couples. For Neumann coupling the number of rows equals the number of strain components  $\boldsymbol{\varepsilon}$  and the number of additional semi-Dirichlet coupling conditions.

Especially for fine micro discretizations with many boundary nodes the system of equations for Neumann coupling will be smaller than for Dirichlet and periodic coupling.

For Dirichlet and periodic coupling the system of equations has to be solved only once, for Neumann coupling realized by the semi-Dirichlet approach the set of equations has to be solved in each of the iterations.

It should be mentioned that at least for Dirichlet and periodic coupling conditions the method of Lagrange multipliers can be realized by the more efficient direct use of the macroscopic displacement field.

Coupling	Direct solution method	Lagrange multiplier method
Dirichlet	$2 \cdot (N - 2)^2$	$2 \cdot (N^2 + 4(N - 1))$
Periodic	$2 \cdot ((N - 2)^2 + (N - 1) + (N - 2))$	$2 \cdot (N^2 + N + (N - 1))$

**Table 1: Comparison of the degrees of freedom in 2D:** Direct solution method versus Lagrange multiplier method for Dirichlet and periodic coupling.

For a uniform micro mesh in 2D with  $N$  nodes per edge Tab. 1 displays the number of degrees of freedom for both methods in the cases of Dirichlet and periodic coupling conditions. Especially for Dirichlet coupling the direct solution of the microproblem is a convenient option. The number of degrees of freedom for the direct implementation of Dirichlet coupling is reduced to those of the  $(N - 2)^2$  nodes in the interior of the microdomain, whereas for the Lagrange multiplier method not only the degrees of freedom of the  $N^2$  nodes have to be considered, but additionally the degrees of freedom to impose the coupling conditions on the  $4(N - 1)$  boundary nodes. Furthermore, Dirichlet coupling conditions can be easily realized by means of static condensation.

## 4 A priori error estimates and a posteriori error estimation

This section 4 provides the unified a priori estimates covering the macro error, the micro error and the modeling error. Moreover, the recovery-type error estimator of Zienkiewicz-Zhu based on superconvergent stress and strain is introduced and contrasted to error computation based on reference solutions.

### 4.1 A priori estimates

FE-HMM as a particular instance of the most general Heterogeneous Multiscale Method HMM E and Engquist [2003], E, Engquist, and Huang [2003], E et al. [2007], Abdulle et al. [2012] has its foundation in mathematical homogenization by asymptotic expansion, Bensoussan et al. [1976], Sanchez-Palencia [1980], Allaire [1992], Cioranescu and Donato [1999].

A priori estimates for various types of partial differential equations (PDEs) have been derived for FE-HMM by virtue of its foundation in mathematical homogenization; for the elliptic case we refer to E et al. [2005], Ohlberger [2005], for the elliptic case of linear elasticity in a geometrical linear setting to Abdulle [2006], Abdulle [2009]. A posteriori error analysis along with upper and lower bounds of a residual-based error estimator have been presented in Abdulle and Nonnenmacher [2011], for an adaptive strategy governed by quantities of interest we refer to Abdulle and Nonnenmacher [2013].

The total FE-HMM error can be decomposed into three parts

$$\|\mathbf{u}^0 - \mathbf{u}^H\| \leq \underbrace{\|\mathbf{u}^0 - \mathbf{u}^{0,H}\|}_{e_{mac}} + \underbrace{\|\mathbf{u}^{0,H} - \tilde{\mathbf{u}}^H\|}_{e_{mod}} + \underbrace{\|\tilde{\mathbf{u}}^H - \mathbf{u}^H\|}_{e_{mic}}, \quad (41)$$

where  $e_{mac}$ ,  $e_{mod}$ ,  $e_{mic}$  are the macro error, the modeling error, and the micro error.

Here,  $\mathbf{u}^0$  is the solution of the homogenized problem (4),  $\mathbf{u}^H$  is the FE-HMM solution,  $\mathbf{u}^{0,H}$  is the standard (single-scale) FEM solution of problem (5) that is obtained through exact  $\mathbb{A}^0$ ; and  $\tilde{\mathbf{u}}^H$  is the FE-HMM solution obtained through exact microfunctions (in  $W(K_l)$ ).

For sufficiently regular problems the following a priori estimates hold in the  $L^2$ -norm, the  $H^1$ -norm and the energy-norm (definition of these norms in Appendix A.2):

$$\|\mathbf{u}^0 - \mathbf{u}^H\|_{L^2(\mathcal{B})} \leq C \left( H^{p+1} + \left( \frac{h}{\epsilon} \right)^{2q} \right) + e_{mod}, \quad (42)$$

$$\|\mathbf{u}^0 - \mathbf{u}^H\|_{H^1(\mathcal{B})} \leq C \left( H^p + \left( \frac{h}{\epsilon} \right)^{2q} \right) + e_{mod}, \quad (43)$$

$$\|\mathbf{u}^0 - \mathbf{u}^H\|_{A(\mathcal{B})} \leq C \left( H^p + \left( \frac{h}{\epsilon} \right)^{2q} \right) + e_{mod}. \quad (44)$$

For  $e_{mod}$  in (42)–(44) it holds

$$e_{mod} = \begin{cases} 0 & \text{for periodic coupling with } \delta/\epsilon \in \mathbb{N} \\ C \frac{\epsilon}{\delta} & \text{for Dirichlet coupling with } \delta > \epsilon. \end{cases} \quad (45)$$

given that the hypotheses hold, that the elasticity tensor  $\mathbb{A}^\epsilon$  is periodic on the RVE and, that the micro solution is sufficiently smooth, Jecker and Abdulle [2016].

The modeling error for Dirichlet coupling in (42)–(44) is due to boundary layers E et al. [2005] (Thm. 1.2), Abdulle [2009]. So even for  $H \rightarrow 0$  and  $h \rightarrow 0$  there is a residual error.

**Remark 1**

(i) Order  $2q$  of the micro error in the  $L^2$ -norm according to (42) seems to contradict standard FEM results. Even more, its order each in the  $H^1$ - and energy- norms scales with  $2q$  in the same order as in the  $L^2$ -norm, a phenomenon which is referred to as *superconvergence* in the context of standard (single-scale) finite element methods. For the latter however, superconvergence is not unconditional, since that kind of superconvergence is not only restricted to particular element sites but also to the rectangular shape of them Barlow [1976]. Notice that the latter superconvergence can be used for the construction of a recovery-type error estimator based on the so-called Superconvergent Patch Recovery (SPR) introduced by Zienkiewicz and Zhu [1992a], Zienkiewicz and Zhu [1992b], a concept which is adopted in Sec. 4.3 of the present work.

(ii) The alleged inconsistency of the micro convergence error order is resolved by the fact that (42)–(44) describe the micro error as propagated to the macroscale; it is measured by macro quantities, i.e. by  $\mathbf{u}^H$  in the  $L^2$ -norm, and by macroscopic stress and strain in the energy-norm. In contrast to this propagated micro error on the macroscale, the micro error on the microscale, which is measured by micro quantities, scales in the order of  $\mathcal{O}((h/\epsilon)^{q+1})$  in the  $L^2$ -norm and of  $\mathcal{O}((h/\epsilon)^q)$  in the  $H^1$ - and energy-norm thus being consistent with estimates of standard finite elements.

(iii) For its composition covering both the macro error as well as the micro error, the estimates (42)–(44) enable strategies to achieve the optimal convergence order for minimal computational costs in uniform micro-macro discretizations; they answer the practical question on how to improve in two-scale finite element frameworks the accuracy by  $H - /h$ -refinements on both the macro- and the microscale most efficiently.

macro-,micro-FEM	$L^2$ -norm	$H^1$ -/energy-norm
$P^p, P^q$	$N_{mic} = (N_{mac})^{p+1/2q}$	$N_{mic} = (N_{mac})^{p/2q}$

**Table 2:** Optimal uniform micro-macro refinement strategies: full order for minimal effort.  $N_{mic}$  denotes the number of unknowns on the microscale,  $N_{mac}$  on the macroscale.

Table 2 displays the optimal uniform micro-macro refinement strategies for the error in the  $L^2$ -norm and the  $H^1$ -/energy-norm. Of course, the strategy’s dependency on the polynomial order of macro shape functions  $p$  and  $q$  on the microscale crucially relies on sufficient regularity of the corresponding BVPs.

(iv) For numerical convergence analyses of the macro error it is enough to compute the total error at various macrodiscretizations  $H$  keeping the micro errors constant by employing a constant micro discretization  $h$ . Consequently, the reference solution for error computation is  $\mathbf{u}^{H,\text{ref}}(H \rightarrow 0, h = \text{const.})$ . Convergence analyses of the micro error are carried out analogously; in this case the reference solution is  $\mathbf{u}^{H,\text{ref}}(H = \text{const.}, h \rightarrow 0)$ .

(v) To our knowledge no estimate for the modeling error along with Neumann BC is available in mathematical literature.

## 4.2 Error computation

For the special case of a micro error convergence analysis on the microscale (as e.g. on a selected microdomain) any macroscopic influence must be switched off. However, since different micro discretizations imply numerical differences in the stiffness approximation, they influence macroscopic displacements, which themselves influence through the post-processing the microscopic quantities. Consequently, for the micro error analysis on the microscale the macrosolution is kept fixed and only the postprocessing is executed and enters the micro error analysis.

Since the estimates (42)–(44) are carried out on the macroscale and measured in macroscopic quantities, error analyses for their numerical verification equally operate on the macroscale.

The integrals for error calculation in the norms (A.4)–(A.6) are approximated by numerical integration of Gauss-Legendre. The computations are carried out on macro element level of the discretization for the reference solution. For the error in the  $L^2$ -norm it follows

$$\|\mathbf{u}^{H,\text{ref}} - \mathbf{u}^H\|_{L^2(\Omega)} = \left[ \sum_{K \in \mathcal{T}_{\text{ref}}} \left( \sum_{i=1}^{ngp} \omega_i (\mathbf{u}^{H,\text{ref}}(\mathbf{x}_i^{\text{ref}}) - \mathbf{u}^H(\mathbf{x}_i^{\text{ref}}))^2 \det \mathbf{J} \right) \right]^{1/2}. \quad (46)$$

For evaluating (46) the displacements of both the standard FE-HMM solution  $\mathbf{u}^H$  and the reference solution  $\mathbf{u}^{H,\text{ref}}$  have to be known in the quadrature points of the reference solution  $\mathbf{x}_i^{\text{ref}}$ . In the simplest case –when only the micro error convergence is analyzed– both solutions are computed on the same macro discretization  $\mathcal{T}_{\text{ref}} = \mathcal{T}_H$  and the elements and their quadrature points therefore coincide, cf. Remark 1 (iv).

If the macro error or the total error is investigated, the reference solution has a finer macro triangulation than the single FE-HMM solutions. In this case the results of the FE-HMM solution are projected onto the finer grid of the reference solution.

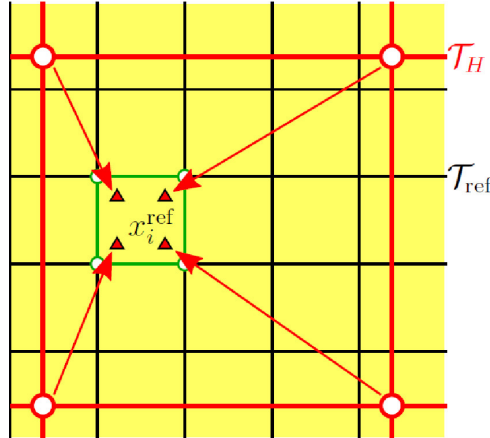


**Figure 4:** Projection from a coarse macro mesh (red) onto the quadrature points of an element (green) in the fine mesh of the reference solution (black) for linear shape functions.

Figure 4 schematically displays the projection from a rather coarse macro triangulation  $\mathcal{T}_H$  onto the finer reference triangulation  $\mathcal{T}_{\text{ref}}$  for one element of the reference mesh. Therein,

the quantities of the coarse mesh are projected onto the quadrature points of the reference solution  $x_i^{\text{ref}}$  such that the error of the quantities of interest can be calculated, e.g. for the displacement error in the  $L^2$ -norm according to (46).

If the absolute figures of the errors are of interest, the total discretization error, its macro and micro parts can be efficiently computed by merely two reference solutions as for example in Tab. 3.

step	type of error	reference solution $\mathbf{u}^{H,\text{ref}}$
1.)	total error at $H$ and $h$ : $e_{\text{tot}}$	$\mathbf{u}^H(H \rightarrow 0, h \rightarrow 0)$
2.)	macro error: $e_{\text{mac}}$	$\mathbf{u}^H(H, h \rightarrow 0)$ .
3.)	resultant micro error: $e_{\text{mic}} = e_{\text{tot}} - e_{\text{mac}}$	$[\mathbf{u}^H(H \rightarrow 0, h)]$

**Table 3:** Rationale for the decomposition of the estimated error into its macro and micro parts.

The computation of reference solutions in 1.) and 2.) in Tab. 3 can efficiently be carried out in single-scale finite element simulations on the macroscale using the homogenized elasticity tensor  $\mathbb{A}^{0,h}(h \rightarrow 0)$  determined in a preprocessing step.

### 4.3 Error estimation based on the Superconvergent Patch Recovery (SPR)

In (engineering) practice, error computation as described in 4.2 is prohibitive. Instead, the total error is estimated, which is carried out on the particular discretization in use. For that purpose the present work uses the recovery-type error estimation of Zienkiewicz and Zhu, which exploits superconvergence of stress and strain. In Zienkiewicz and Zhu [1992a], Zienkiewicz and Zhu [1992b] a procedure for the transfer of the superconvergence property from superconvergent, inner element points to element nodes referred to as "superconvergent patch recovery" (SPR) was proposed. Based on these recovered superconvergent nodal values the same authors constructed an error estimator that guided adaptive mesh refinement.

**4.3.1 The SPR on the macroscale** For ready reference, the rationale of the SPR is briefly re-iterated for linear and quadratic shape functions, where we restrict to the  $n_{\text{dim}} = 2$  case for convenience. Strain and stress are calculated at superconvergent element sites that is for  $p=1$  in the center of a rectangular element, for  $p=2$  in the  $2 \times 2$  points of Gauss-Legendre quadrature. These values are transferred by a least-square procedure to the finite element node in the direct neighborhood, for a visualization see Fig. 5. Elements having such a node in common are referred to as the patch in the superconvergent recovery procedure.

Stresses on the patch are prescribed component-wise by

$$\sigma_p^* = \mathbf{P} \mathbf{a} \quad (47)$$

with, for the case of linear shape functions,

$$\mathbf{P} = [1, x, y, xy] \quad \text{and} \quad \mathbf{a} = [a_1, a_2, a_3, a_4]. \quad (48)$$

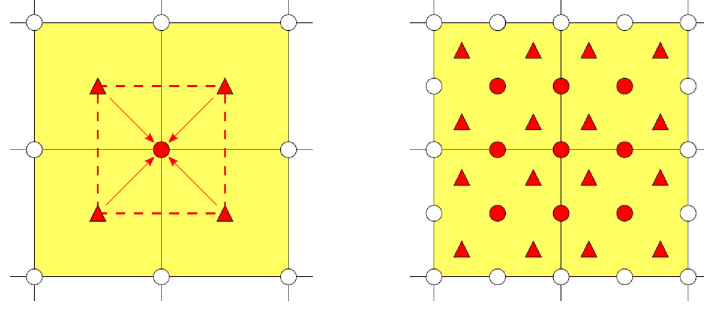


**Figure 5:** Recovery of nodal stresses from stresses of surrounding superconvergent points (marked by a  $\triangle$ ) for 4-node elements (left) and 9-node elements (right). The nodal stresses of the red marked nodes can be calculated using the shown patches.

Vector  $\mathbf{P}$  contains polynomial terms of bilinear shape functions for  $n_{dim} = 2$ , no matter whether it is a 4-node or 9-node quadrilateral, since the patch around a finite element node consists of four superconvergent points in either case. For the determination of the unknown vector  $\mathbf{a}$  the function

$$\begin{aligned} F(\mathbf{a}) &= \sum_{i=1}^n (\sigma_h(x_i, y_i) - \sigma_p^*(x_i, y_i))^2 \\ &= \sum_{i=1}^n (\sigma_h(x_i, y_i) - \mathbf{P}(x_i, y_i)\mathbf{a})^2 \end{aligned} \quad (49)$$

has to be minimized. Therein,  $(x_i, y_i)$  are the coordinates of the superconvergent points,  $n$  is the number of superconvergent points of the total patch and  $\sigma_h(x_i, y_i)$  are the stresses in these superconvergent points. Minimization of  $F(\mathbf{a})$  implies that  $\mathbf{a}$  fulfills the condition

$$\sum_{i=1}^n \mathbf{P}^T(x_i, y_i) \mathbf{P}(x_i, y_i) \mathbf{a} = \sum_{i=1}^n \mathbf{P}^T(x_i, y_i) \sigma_h(x_i, y_i), \quad (50)$$

which can be solved for  $\mathbf{a}$

$$\mathbf{a} = \mathbf{A}^{-1} \mathbf{b} \quad (51)$$

with

$$\mathbf{A} = \sum_{i=1}^n \mathbf{P}^T(x_i, y_i) \mathbf{P}(x_i, y_i) \quad \text{and} \quad \mathbf{b} = \sum_{i=1}^n \mathbf{P}^T(x_i, y_i) \sigma_h(x_i, y_i). \quad (52)$$

Stresses in the central node of the patch can be recovered by inserting its nodal coordinates  $(x_N, y_N)$  into the  $\mathbf{P}$ -vector in (47).

Figure 6 shows the patches for boundary nodes lying either on edges or at corners. Corner nodes adjoin only one element which is insufficient for the calculation method described above. A similar situation arises for any node on the boundary which is adjoined to two elements. Here the patches have to be complemented by further elements.

Another peculiarity exists for patches of 9-node elements. For all of the red marked nodes in Fig. 5 –except of the central-one– there are two or even more patches available to compute the nodal stresses. In this case the nodal values are calculated by simply averaging the results from the single patches.

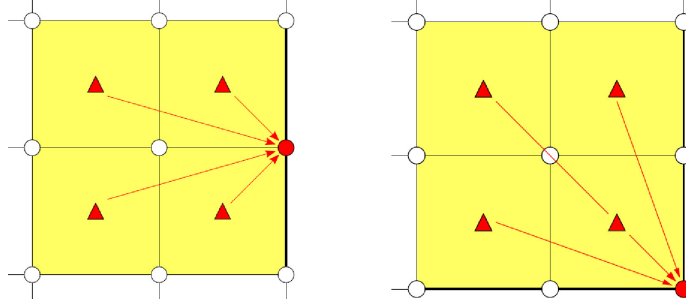


**Figure 6:** Recovery of nodal stresses using patch recovery for boundary and corner nodes.

**4.3.2 Error estimator and effectivity index** As described above, the error estimator is built on superconvergent stress  $\boldsymbol{\sigma}^*$  and strain  $\boldsymbol{\varepsilon}^*$ . Of course, the procedure is not applicable for an error estimate in the  $L^2$ -norm of displacements, since for the existing continuity of displacements the recovery-type error estimator cannot be constructed. The estimated error in the energy-norm reads as

$$\begin{aligned} \|\bar{\mathbf{e}}\|_{A(\Omega)} = \|\mathbf{u}^* - \mathbf{u}^H\|_{A(\Omega)} &= \sqrt{\int_{\Omega} (\boldsymbol{\sigma}^* - \boldsymbol{\sigma}^H) : (\boldsymbol{\varepsilon}^* - \boldsymbol{\varepsilon}^H) dV}, & (53) \\ &\approx \left[ \sum_{K \in \mathcal{T}_H} \left( \sum_{i=1}^{ngp} \omega_i (\boldsymbol{\sigma}^* - \boldsymbol{\sigma}^H)(\mathbf{x}_i^H) : (\boldsymbol{\varepsilon}^* - \boldsymbol{\varepsilon}^H)(\mathbf{x}_i^H) \det \mathbf{J} \right) \right]^{1/2} & (54) \end{aligned}$$

Compared to the error computation based on a reference solution

$$\|\mathbf{e}\|_{A(\Omega)} = \|\mathbf{u}^0 - \mathbf{u}^H\|_{A(\Omega)} \approx \left[ \sum_{K \in \mathcal{T}_{\text{ref}}} \left( \sum_{i=1}^{ngp} \omega_i (\boldsymbol{\sigma}^{\text{ref}} - \boldsymbol{\sigma}^H)(\mathbf{x}_i^{\text{ref}}) : (\boldsymbol{\varepsilon}^{\text{ref}} - \boldsymbol{\varepsilon}^H)(\mathbf{x}_i^{\text{ref}}) \det \mathbf{J} \right) \right]^{1/2} \quad (55)$$

the numerical effort of the error estimation is clearly much smaller, since the integration of the error is carried out on the corresponding macro mesh with triangulation  $\mathcal{T}_H$  instead of the reference mesh with triangulation  $\mathcal{T}_{\text{ref}}$ . More important, error estimation can be carried out on-the-fly, no additional solution on a different mesh is required.

The quality of the error estimator is typically assessed by the so-called effectivity index  $\theta$  which is defined as the ratio of the estimated error  $\bar{\mathbf{e}}$  to the true error  $\mathbf{e}$

$$\theta = \frac{\|\bar{\mathbf{e}}\|}{\|\mathbf{e}\|}. \quad (56)$$

For consistency the effectivity index must tend to unity as the exact error tends to zero which can easily be shown if the error of stress and strain is considered. For the case of stresses entering the error analysis, the effectivity index follows to

$$\theta = \frac{\|\bar{\mathbf{e}}_{\sigma}\|}{\|\mathbf{e}_{\sigma}\|} = \frac{\|\boldsymbol{\sigma}^* - \boldsymbol{\sigma}^H\|}{\|\boldsymbol{\sigma}^0 - \boldsymbol{\sigma}^H\|} = \frac{\|\boldsymbol{\sigma}^* - \boldsymbol{\sigma}^0 + \boldsymbol{\sigma}^0 - \boldsymbol{\sigma}^H\|}{\|\boldsymbol{\sigma}^0 - \boldsymbol{\sigma}^H\|}. \quad (57)$$

The numerator in (57) contains the error of standard stresses with respect to superconvergent stresses. A distinction of cases provides an upper and a lower bound for  $\theta$

$$1 - \frac{\|\boldsymbol{\sigma}^* - \boldsymbol{\sigma}^0\|}{\|\boldsymbol{\sigma}^0 - \boldsymbol{\sigma}^H\|} \leq \theta \leq 1 + \frac{\|\boldsymbol{\sigma}^* - \boldsymbol{\sigma}^0\|}{\|\boldsymbol{\sigma}^0 - \boldsymbol{\sigma}^H\|}. \quad (58)$$

Since the error of superconvergent quantities is expected to converge in higher order than the error of standard quantities, both bounds tend to unity as the error tends to zero.

**Remark 2**

Imagine the case of error estimation on the macroscale for two different (macro-, micro-) discretizations, e.g.  $(H, h)$  and  $(H, h/2)$ ; the figures of the error estimates are expected to differ. Does this difference indicate that the error estimator on the macroscale includes the microdiscretization error? If not, why not and what else is indicated by the difference? Here, the error estimator operates on the macroscale and exclusively estimates the macro discretization error at macro element size  $H$  along with a given micro constitutive law<sup>3</sup>. The micro constitutive law is given in terms of its type and its material parameters, the latter depend on microdiscretization  $h$ . For the present case of linear elasticity the approximation  $\mathbb{A}^{0,h}$  and its coefficients converge for sufficiently regular problems in the order  $\mathcal{O}(h^{2q})$  to  $\mathbb{A}^0$  for  $h \rightarrow 0$  Jecker and Abdulle [2016], Eidel and Fischer [2018]. On the microscale the deviation of  $\mathbb{A}^{0,h/2}$  to  $\mathbb{A}^{0,h}$  indicates a discretization error as the deviation of  $\mathbf{u}^{h/2}$  to  $\mathbf{u}^h$  does, which is hence accessible to an error estimator working on the microscale. In the error estimation working on the macroscale however, the deviation of  $\mathbb{A}^{0,h/2}$  to  $\mathbb{A}^{0,h}$  is not a discretization error but indicates a modeling-type error in terms of different constitutive laws, in the present setting in terms of different model parameters for the same *type* of constitutive law.

## 5 Numerical examples

In this section a thorough convergence and error analysis is carried out for the three coupling conditions employing linear and quadratic shape functions on both the macro- and the microscale.

First, the three micro-coupling conditions are compared in the microscale setting of (i) a matrix-inclusion problem, (ii) a chessboard-type microstructure, and (iii) a sine wave distribution of material stiffness, where the strength and quality of the stiffness contrast between different phases and its impact on the convergence properties is a key aspect of investigation.

The convergence analysis measures the micro error both on the microscale (i.e. on one microdomain) and on the macroscale (as the total micro error that is propagated to the macroscale). Estimates for sufficiently regular problems are provided in Sec. 4.1. For the microerror on the macroscale the order  $2q$  is expected in all three norms, see (42)–(44). For the micro error as measured on the microscale, order  $q + 1$  is expected in the  $L^2$ -norm, and  $q$  in the  $H^1$ - and energy-norm.

Similarly, the regularity of the macro-BVP is examined through the convergence of the

---

<sup>3</sup>Recall, that the reference solution for the computation of the true macro error is  $\mathbf{u}^H(H \rightarrow 0, h)$ .

macro error. Here, the results of a clamped, square plate with low regularity due to notch effects at the clamped boundary are contrasted to a tapered cantilever of proven high regularity.

Moreover, the above examples, which have plane strain conditions and loading by volume forces in common, serve the purpose to compare the estimated error with the true error and to verify the optimal uniform micro-macro mesh refinement strategies of Tab. 2.

### 5.1 Micro convergence analysis

The macro problem common to all micro problems is a square cantilever subject to a volume forces of  $\mathbf{f} = [0, -10]^T [F/L^2]$ . The coupling conditions which will be analyzed are Dirichlet, Neumann and periodic coupling.

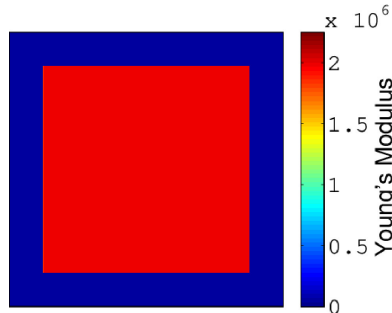


**Figure 7: Matrix-inclusion microstructure.** Distribution of Young's modulus on the micro domain.

**5.1.1 Matrix-inclusion problem** In the first numerical example we consider the microstructure of a stiff inclusion in a soft matrix, which is displayed in Fig. 7. The Young's moduli of the inclusion  $E_i = 200\,000 [F/L^2]$  and the matrix phase  $E_m = 40\,000 [F/L^2]$  exhibit a contrast of  $E_i/E_m = 50$ , for the Poisson's ratio it holds  $\nu = 0.2$ . The volume ratio of the inclusion phase is  $V_i/V_{tot} = 9/16$ . The square RVE exhibits side length  $\epsilon = 0.005$ , which is maintained for all examples in the present work.

The simulation results for linear shape functions are displayed in Fig. 8 (first row). The different coupling conditions show minor deviations from each other in the convergence order. The values of the calculated errors are in good agreement between all coupling conditions, only the error for Neumann coupling in the energy-norm is slightly larger. Notice that we use here and in the following relative errors, i.e.  $\|\mathbf{e}\|_{(\Omega)}/\|\mathbf{u}\|_{(\Omega)}$ .

The observed order reduction from theoretical order  $2q = 2$  for  $q = 1$  to approximately 1.4 in all three norms is due to the stiffness-jump at the inclusion-matrix interface along with the high contrast of the Young's moduli of the two phases, the corresponding notch effect lowers the regularity of the microproblem.

The diagrams in Fig. 8 (second row) display the simulation results for quadratic shape functions,  $p=q=2$ . In all of the above described aspects we observe even quantitatively almost the same behavior as for  $p=q=1$ . Hence, it is the singularity of the problem which overrules the theoretical convergence order, i.e. quadratic shape functions do not cure the problem of low regularity.

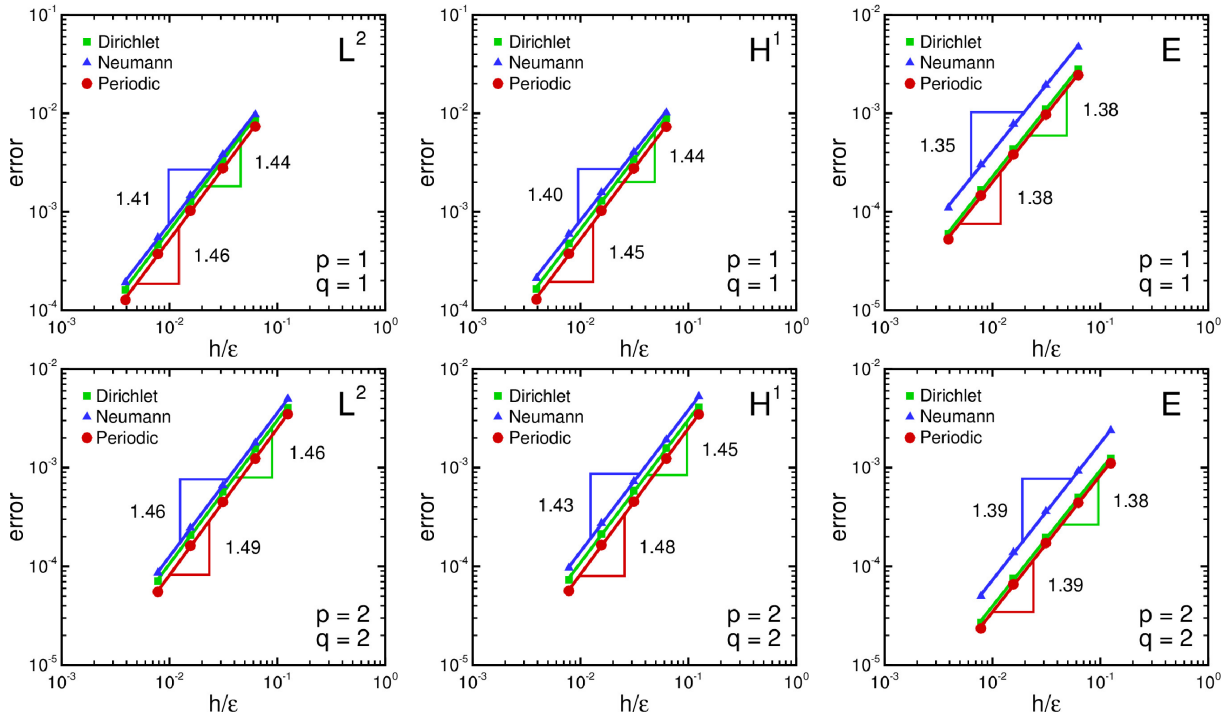


**Figure 8: Micro error convergence on the macroscale for matrix-inclusion problem:** (first row) linear shape functions  $p=q=1$ , (second row) quadratic shape functions  $p=q=2$ , from left to right:  $L^2$ -,  $H^1$ -, energy-norm.

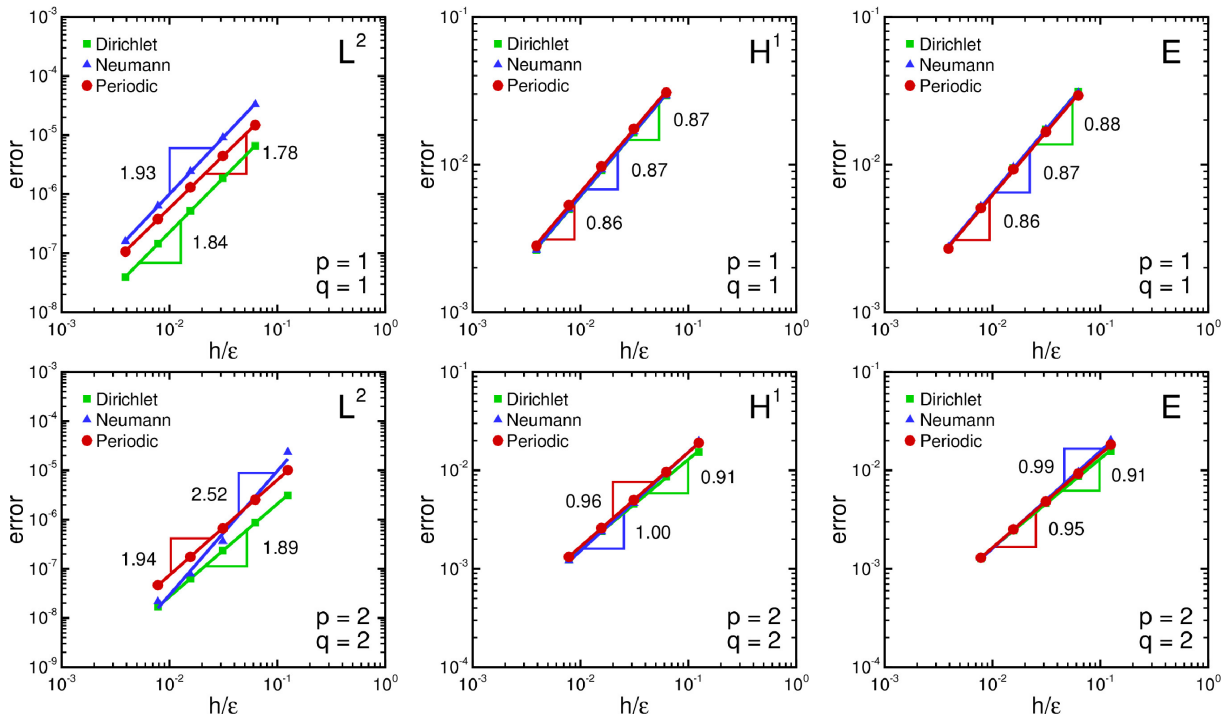


**Figure 9: Micro error convergence on the microscale for matrix-inclusion problem.** (first row) linear shape functions, (second row) quadratic shape functions, (from left to right:)  $L^2$ -,  $H^1$ - and energy-norm.

**Micro error convergence on the microscale.** The results of an error calculation on one microdomain attached to the macroscopic quadrature point at  $[0.26, 0.26]$  is shown in the first row diagrams of Fig. 9 for linear shape functions. The convergence orders for different coupling conditions are in good agreement with each other.

The optimal convergence orders of  $q + 1$  in the  $L^2$ -norm and  $q$  in the  $H^1$ - as well as in the energy-norm is not reached due to the above mentioned reduced regularity.

Figure 9 (second row diagrams) displays the errors on one microdomain for quadratic shape functions. Again the convergence orders of the different coupling conditions are in good agreement with each other except of for Neumann coupling in the  $L^2$ -norm. A closer look at these calculated errors reveals that for coarse discretizations the error is too large and for that reason converges faster than expected. If only the two finest discretizations are considered, convergence is in reasonable agreement with the other two coupling conditions.

### 5.1.2 Comparison of methods for constant traction BC: semi-Dirichlet coupling versus perturbation technique

As described in Sec. 3.3 two different techniques are considered and compared, which fulfill the constant traction BC and remove the rigid body motions from the RVE. The methods are the semi-Dirichlet coupling introduced by Javili et al. [2017] and the perturbation technique going back to Miehe and Koch [2002]. For a comparison of the methods the above matrix-inclusion problem is considered but for visualization purposes the applied load and the microdomain size are increased compared to Sec. 5.1.1. The methods are compared, first with respect to their accuracy, second with respect to kinematical implications of removing the rigid body motions from the RVE.

$p=q$	$h/\epsilon$	1/16	1/32	1/64	1/128	1/256
1	semi-Dirichlet [in $10^{-6}$ ]	28.3848	28.4078	28.4151	28.4173	28.4180
	perturbation [in $10^{-6}$ ]	28.3848	28.4078	28.4151	28.4173	28.4180
2	semi-Dirichlet [in $10^{-6}$ ]	28.5173	28.5265	28.5286	28.5291	28.5292
	perturbation [in $10^{-6}$ ]	28.5173	28.5265	28.5286	28.5291	28.5292

**Table 4: Constant traction BC: Comparison of semi-Dirichlet coupling and perturbation technique.**  $L^2$ -normed solution vector at different micro discretizations for linear and quadratic shape functions.

First and foremost, both methods accurately fulfill the constant traction BC. Table 4 shows the  $L^2$ -norm of the solution vectors in the RVE for the two methods indicating that they yield the same results for various discretizations. For the perturbation technique, the parameters are chosen randomly with a maximum value of  $10^{-5}$ . If the perturbation parameter is varied in the range from  $10^{-8}$  to  $10^0$  for linear shape functions (and in the range of  $10^0$  to  $10^{-7}$  for quadratic shape functions), the results show only minor deviations for the large perturbation parameter. For the choice of  $10^{-1}$  in the case of linear shape functions the  $L^2$ -norm for  $h/\epsilon = 1/256$  amounts to 28.4179, for  $10^0$  to 28.4050.

Figure 10 (left) displays for the semi-Dirichlet coupling the macroelement and the RVE at the lower left quadrature point in the undeformed and deformed configurations. For that case the micro displacements obviously fit into the macroscopic displacement field. Figure 10 (center) similarly displays the same macroelement and RVE for the perturbation

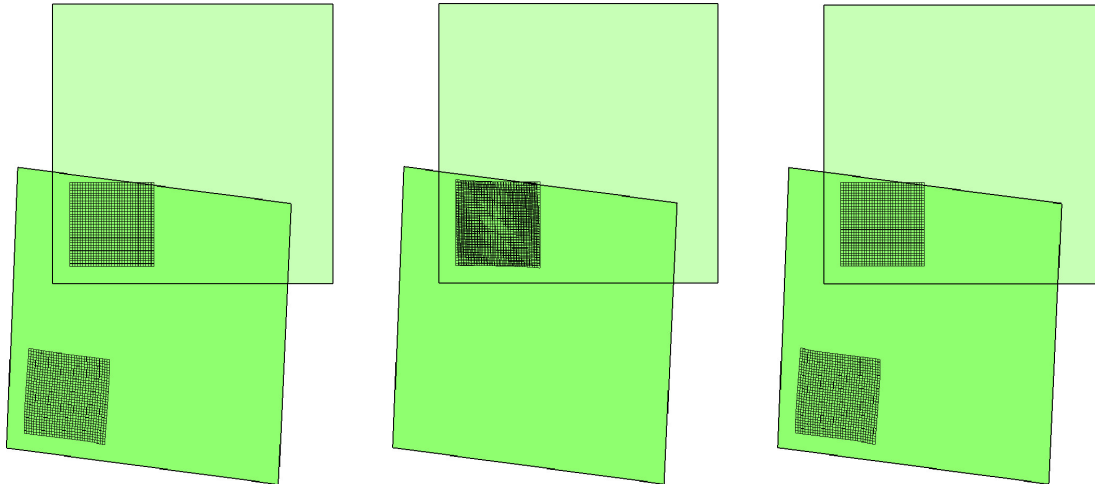


**Figure 10: Micro displacements for matrix-inclusion problem at constant tractions BC** Deformed and undeformed macroelement and microdomain for (left) semi-Dirichlet coupling and for the perturbation technique (center) without and (right) with adding macroscopic rigid body motions.

technique. It is obvious that the calculated micro displacements lack the rigid body motions following from the macroscopic deformation. In order to add the missing kinematical embedding, the displacement of the corresponding macroscopic quadrature point and the rotation of the macroscopic element can be added to the calculated micro displacement field, which results in the deformed configuration of Fig. 10 (right).

An important aspect is the efficiency of the two methods. It is obvious that the semi-Dirichlet coupling is more expensive due to the fact that the system of equations has to be solved more than once in contrast to the perturbation technique.

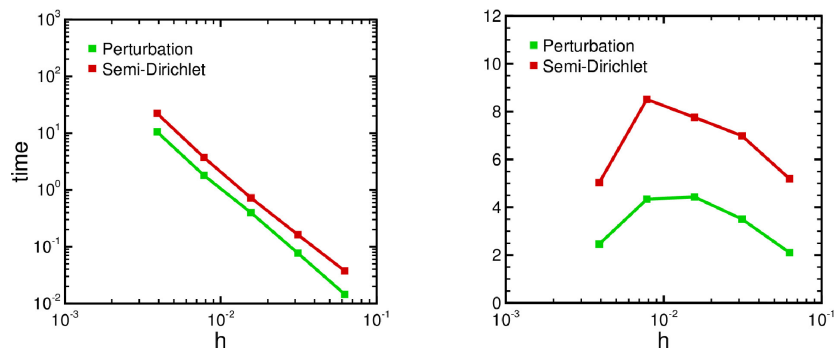


**Figure 11: Computational time for perturbation technique and semi-Dirichlet.** Absolute computational time (left) and relative percentage of computational time related to full computation time on the micro level.

Figure 11 displays the computational times of both methods, with absolute values in the left and, in the right, the percentage of the total computational time (including the stiffness matrix calculation) on the micro level. The results show that there is a difference between the two methods.

In conclusion, both techniques accurately fulfill the constant traction BC and yield the same microscopic stresses and strains. The perturbation technique is accurate for a wide range of the perturbation parameters. In this context it should also be mentioned that

the semi-Dirichlet coupling method is robust with respect to the choice of the nodes in the RVE to which the additional Dirichlet constraints are applied. The only difference between both methods is the embedding of the rigid body motions following from the macroscopic displacements in the semi-Dirichlet technique. For the calculation of the microdisplacements which are used in the transformation matrix (17) it does not matter that the perturbation technique lacks the rigid body motions. If not only microscopic stresses and strains are of interest but equally the microscopic displacements including the macroscopic displacement state, either semi-Dirichlet coupling can be used or the perturbation technique along with rigid body motions enriched kinematics as detailed above. The lower numerical effort favors the iteration-free perturbation technique.

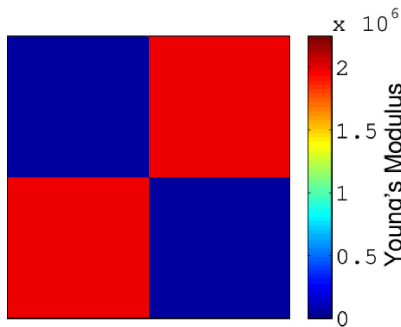


**Figure 12: Chessboard-type microstructure.** Distribution of Young's modulus on the micro domain.

**5.1.3 Chessboard microstructure** While in the first example of the matrix-inclusion problem the material at the RVE boundary was homogeneous, we choose a chessboard-type microstructure, where the heterogeneity is expanded from the micro domain's interior to its boundaries, see Fig. 12. The aim is to investigate the impact of micro-coupling conditions on the results for that case.

The chessboard pattern of Young's modulus distribution exhibits two phases with  $E_1 = 2000000 [F/L^2]$  and  $E_2 = 40000 [F/L^2]$ . The stiffness contrast of the phases is  $E_1/E_2 = 50$ , for the Poisson's ratio it holds  $\nu = 0.2$ .

The results for linear shape functions are displayed in Fig. 13 (first row). Again, the different coupling conditions agree well in the convergence order. The relative error however exhibits larger deviations between the coupling conditions. An exception is the energy-norm for PBC which leads to far worse results. Starting with the coarse discretizations on the right side of Fig. 13 (first row, right) the error first increases with finer meshes and finally decreases again. The results of the calculations with rather fine micro meshes fit well into the results for Dirichlet and Neumann coupling, while the calculated errors for coarse meshes seem to be too small.

Again the optimal convergence order can not be reached in any of the norms due to the reduced regularity of the micro problem which is again based in the stiffness-jump at the interface between the two phases. The deviation from the optimal convergence order is even larger compared to the matrix-inclusion problem.

**Remark:** The convergence results for PBC in the energy-norm deserve a closer investigation; the analysis reveals that stresses in the macroscopic quadrature points do not exhibit sufficient accuracy. The entries of the homogenized elasticity tensor  $\mathbb{A}^0$ , which is

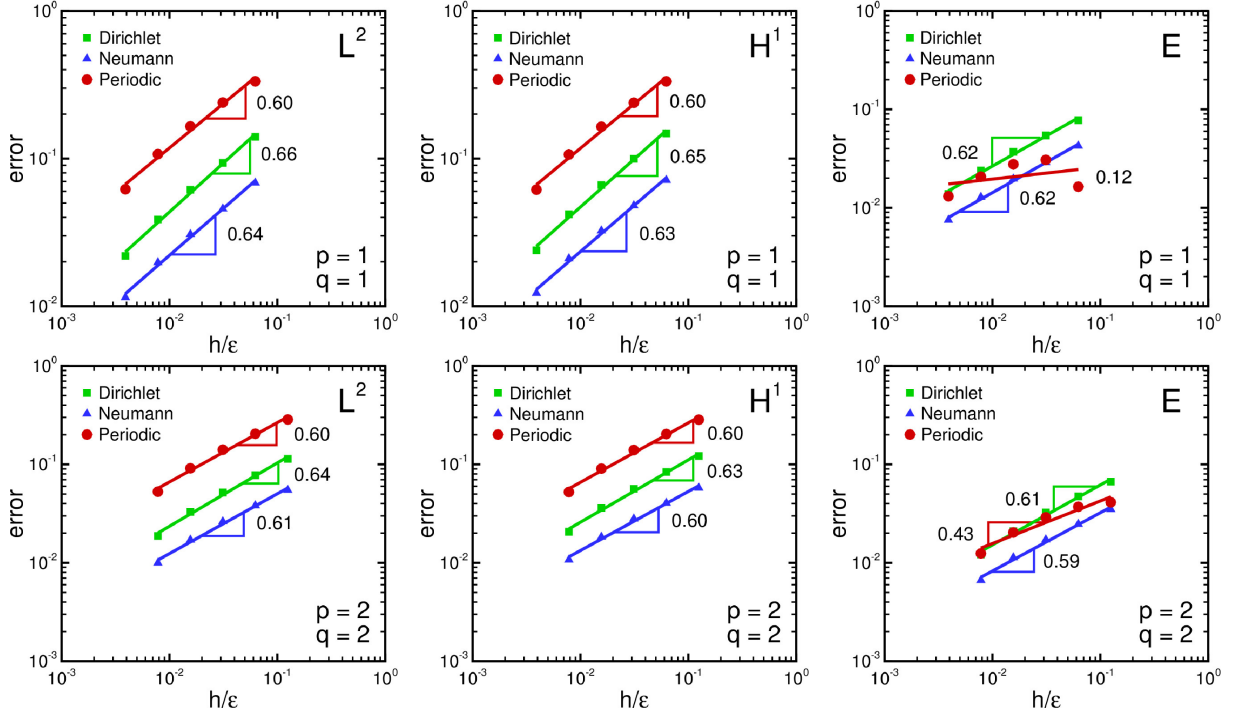


**Figure 13: Micro error convergence on the macroscale for chessboard stiffness pattern.** (first row) linear shape functions,  $p=q=1$ , (second row) quadratic shape functions,  $p=q=2$ , (from left to right:)  $L^2$ -,  $H^1$ -and energy-norm.

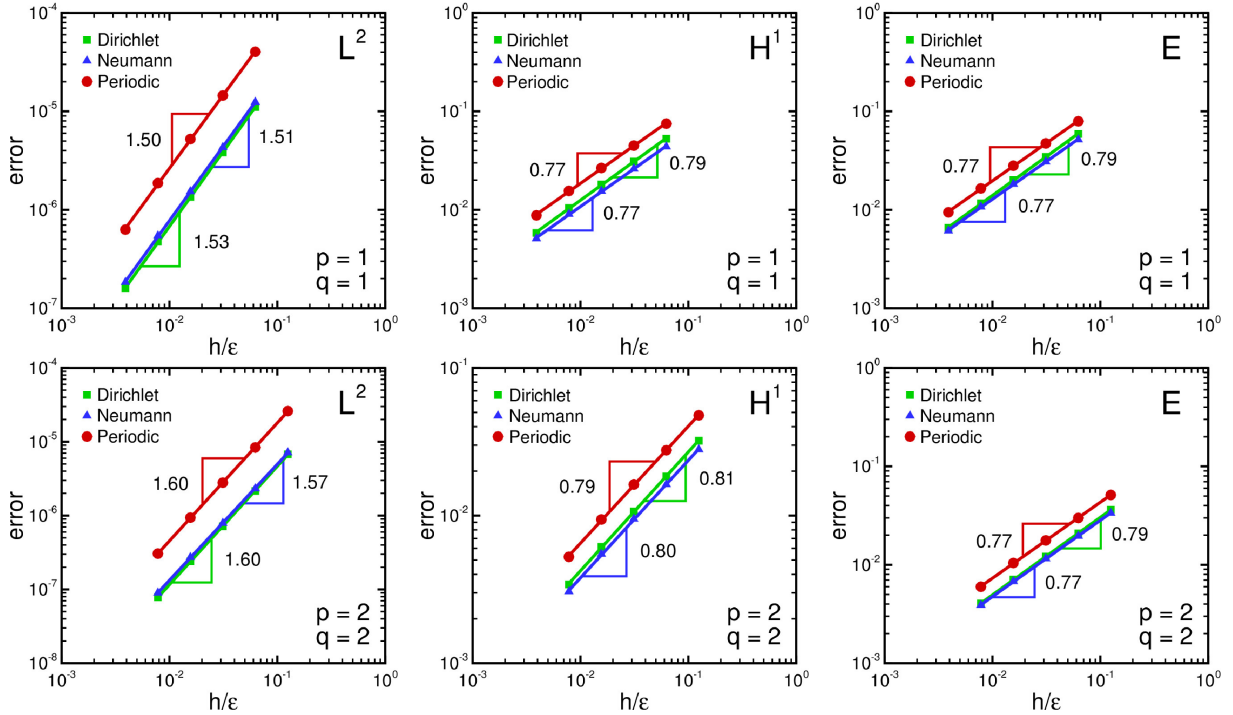
used to calculate macroscopic stresses, converge with orders in the range from 0.62 ( $A_{12}^0$ ) to 0.72 ( $A_{11}^0$ ) which is in the range of the convergence orders of the  $L^2$ - and  $H^1$ -norm. The investigation of the homogenized elasticity tensor showed that there is a major absolute error in the single entries. The error of the coarsest discretization is about 50% of the numerical values of the reference solution in all entries. For Neumann coupling in contrast, the errors are in the range from 7–12%, and for Dirichlet coupling in the range of 8–21%. These findings suggest that the questionable results for the error in the energy-norm for PBC is caused by the major absolute error of the homogenized tensor.

Figure 13 (second row) shows the results for quadratic shape functions. The results do not differ significantly from the results for linear shape functions. Again the error in the energy-norm seems to be too small for periodic coupling conditions and rather coarse discretizations.

The optimal convergence order of  $2q = 4$  is clearly missed and the use of quadratic shape functions does not improve the convergence order.

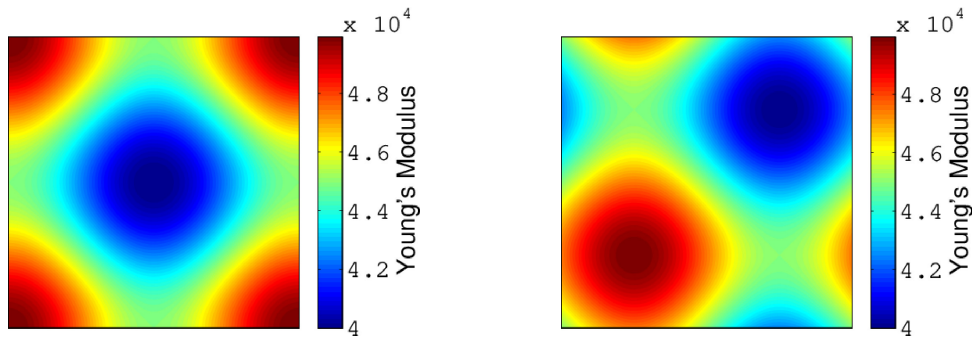
**Micro error convergence on the microscale.** The results of an error calculation on the microdomain related to the macroscopic quadrature point at  $[0.26, 0.26]$  with linear shape functions can be found in Fig. 14 (first row). The convergence orders for different coupling conditions exhibit good agreement.

Figure 14 (second row) indicates that for quadratic shape functions the convergence orders are in good agreement for the different coupling conditions. The convergence order however is not improved for quadratic shape functions compared to the linear case, which is due to the low regularity.



**Figure 14: Micro error convergence on the microscale for chessboard stiffness pattern.** (first row) linear shape functions,  $p=q=1$ , (second row) quadratic shape functions,  $p=q=2$ , (from left to right:)  $L^2$ -,  $H^1$ -and energy-norm.

**5.1.4 Sine wave distribution** The low regularity of the micro BVP in the first two examples is the reason why convergence for quadratic shape functions shows a strong deviation from the nominal order. Aiming at the full convergence order of  $2q$  for the micro error a sine wave-type Young's modulus distribution is chosen, which is expected to exhibit high regularity for its smooth stiffness distribution. Therein, the minimum Young's modulus is  $E_{min} = 40000 [F/L^2]$ , the maximum is  $E_{max} = 50000 [F/L^2]$ .



**Figure 15: Sine wave distribution problem.** Distribution of Young's modulus on (left) a unit cell with cubic symmetry and (right) an alternative unit cell.

The Young's modulus distribution on the micro domain is depicted in Fig. 15. The unit cell in the left reflects the cubic symmetry of the periodic structure; an alternative definition (among many others) of the unit cell is displayed on the right of Fig. 15. While the stiffness results for Neumann and Dirichlet coupling depend on the choice of the unit cell, for PBC stiffness is invariant with respect to that choice. In the following we use the unit cell in the right of Fig. 15.

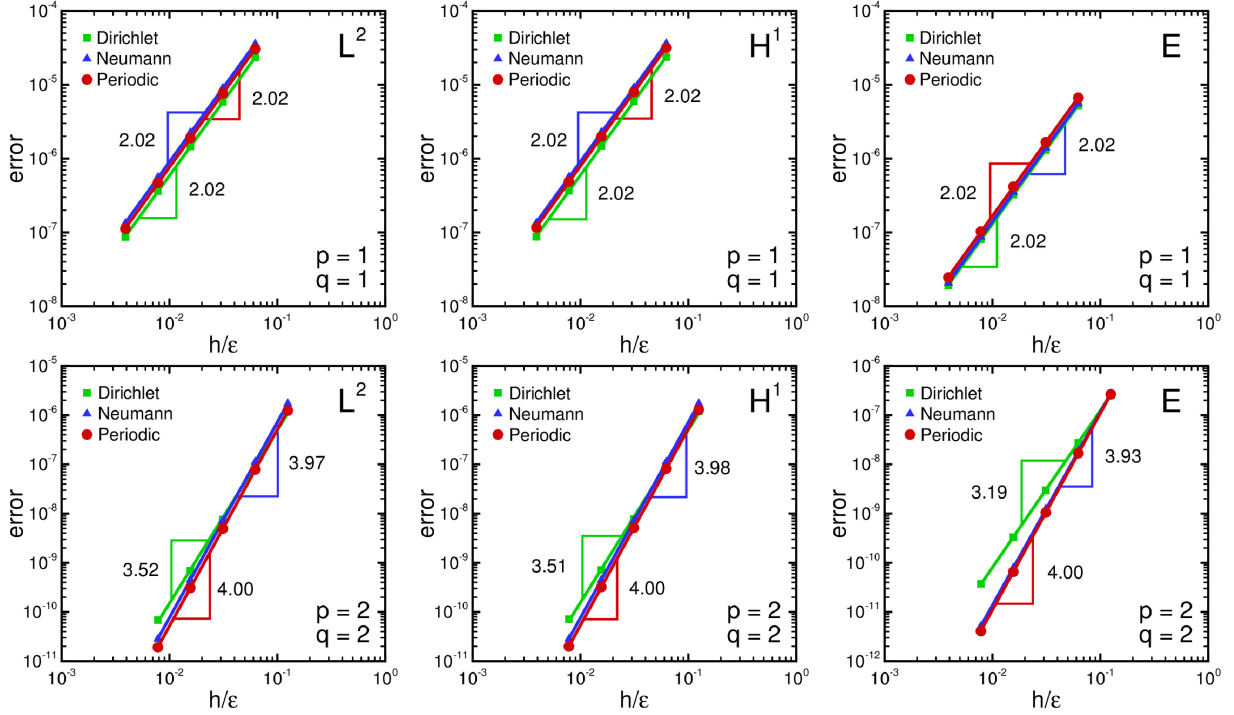


**Figure 16: Micro error convergence on the macroscale for a microstructure with sine wave stiffness distribution.** (first row) linear shape functions,  $p=q=1$ , (second row) quadratic shape functions,  $p=q=2$ , (from left to right:)  $L^2$ -,  $H^1$ - and energy-norm.

Figure 16 (first row) shows the results for linear shape functions. In all norms and for all coupling conditions the convergence order of the calculated errors is 2.02. The numerical values of the relative errors also show only minor deviations. The sine wave distribution enables full regularity of the solution as indicated by the full theoretical convergence order in all norms.

The results for quadratic micro shape functions are displayed in the second row of Fig. 16. For periodic and Neumann coupling conditions the optimal convergence order of  $2q = 4$  is virtually achieved in all norms, while for Dirichlet coupling a reduced order is observed. The numerical values of the relative errors of Neumann and periodic coupling are in good agreement, while the values for Dirichlet coupling exhibit good agreement with the estimates only for coarse discretizations, for finer discretizations they worsen most notably in the energy-norm.

In conclusion, the regularity of the micro BVP enables full convergence order and –opposed to the first two examples– a higher convergence order for quadratic shape functions than for linear shape functions.

**Micro error convergence on the microscale.** The error calculation on the microdomain related to the macroscopic quadrature point at  $[0.26, 0.26]$  for  $q = 1$  yields the results that are displayed in Fig. 17 (first row). The convergence orders of  $q + 1$  in the  $L^2$ -norm and  $q$  in the  $H^1$ - and energy-norm are achieved for Dirichlet and periodic coupling, for Neumann coupling there are some minor deviations in the  $L^2$ -norm.

The results of the error calculation on the same microdomain for quadratic shape functions are displayed in Fig. 17 (second row). For periodic coupling the optimal convergence order is achieved in all norms, for Neumann coupling the optimal convergence order is restricted

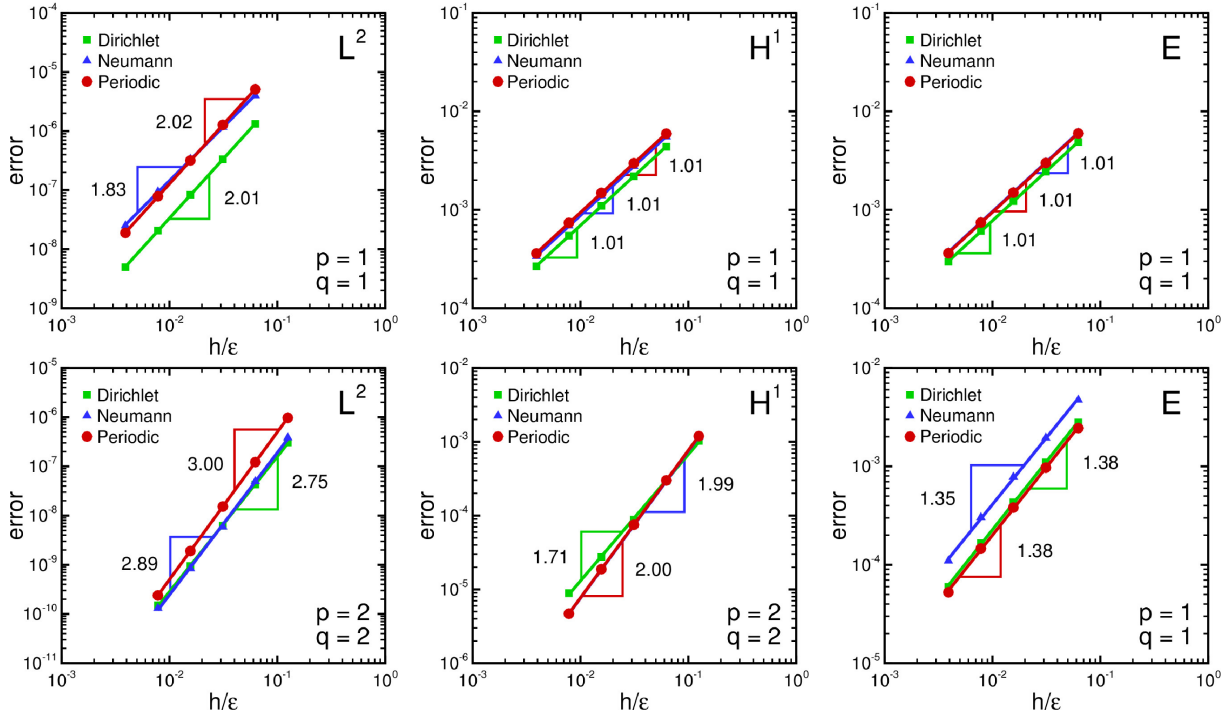


**Figure 17: Micro error convergence on the microscale for a microstructure with sine wave stiffness distribution.** (first row) linear shape functions  $p=q=1$ , (second row) quadratic shape functions  $p=q=2$ , (from left to right:)  $L^2$ -,  $H^1$ -, and energy-norm.

to the  $H^1$ - and the energy-norm. Dirichlet coupling however, shows again minor reductions in all three norms, which is consistent with the reduced convergence order of the micro error on the macroscale.

**Remark:** The measured convergence orders being almost in perfect agreement with the a priori estimates could suggest that the observed regularity is due to the low stiffness contrast (1:1.25). Additional analyses employing an increased stiffness contrast of up to 1:25 yield the same convergence orders and thereby rebut this hypothesis. Instead it is the smoothness of Young's modulus distribution that enables the regularity in terms of full convergence orders.

## 5.2 Macro convergence analysis

After the assessment of micro errors both on the micro as well as on the macroscale, the macro error convergence is investigated in the following.

**5.2.1 Square cantilever** In the first numerical example we consider the square cantilever of Fig. 18, which is subject to volume forces of  $\mathbf{f} = [0, -10]^T [F/L^2]$ . The microstructure is the already introduced sine wave-type distribution of Young's modulus.

The results of the convergence analysis for linear shape functions is shown in the first row of Fig. 19. The optimal convergence orders, of  $p + 1$  in the  $L^2$ -norm and of  $p$  in the  $H^1$ - and energy-norm are not achieved, but the deviations are small. The micro-macro coupling condition has virtually no influence on the macro error convergence. The results employing quadratic shape functions as displayed in Fig. 19 (second row) exhibit

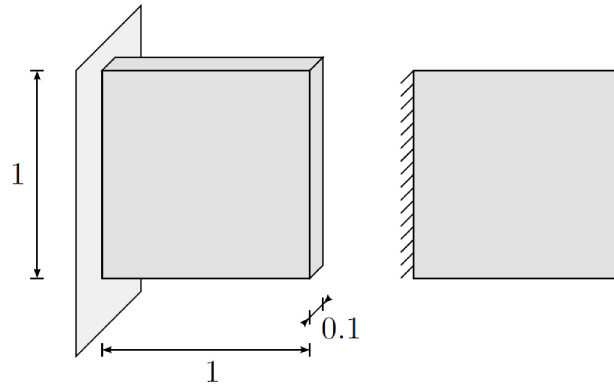


Figure 18: Model of a square cantilever.

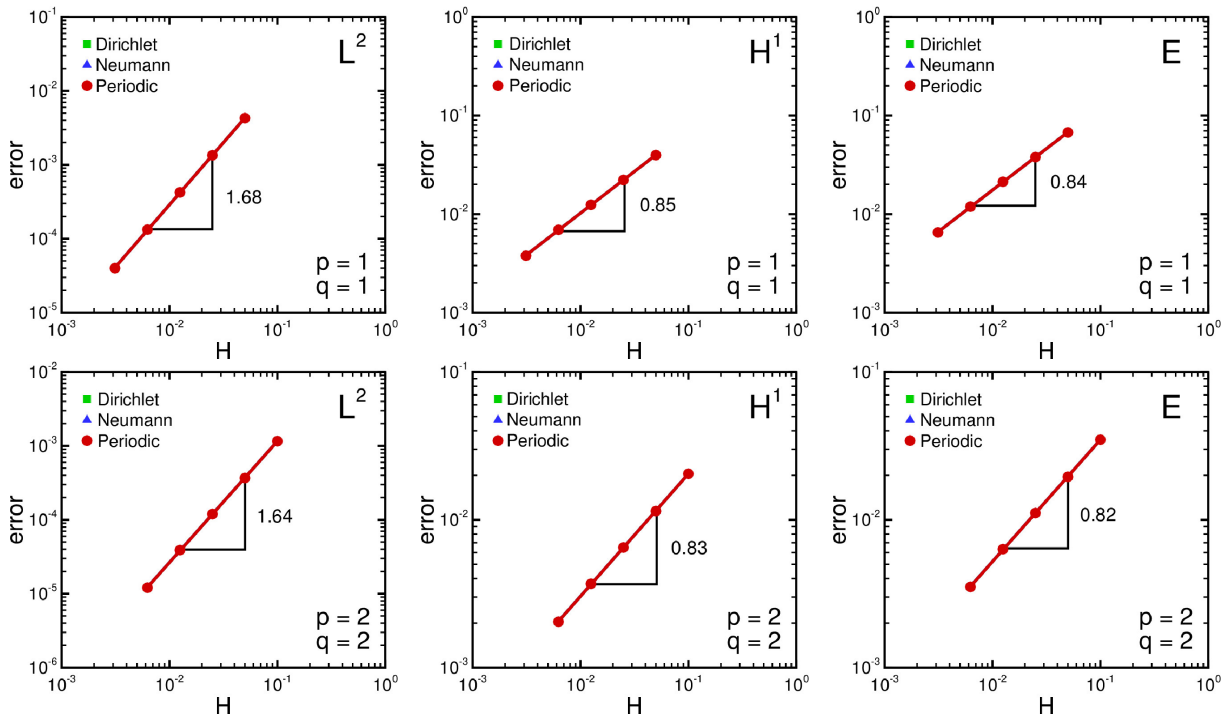
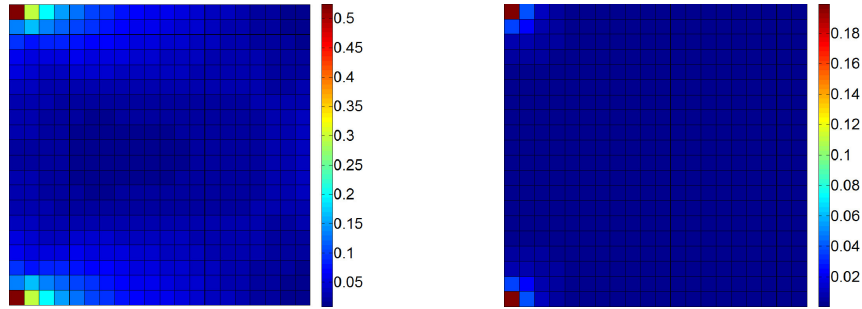


Figure 19: Macroconvergence for square cantilever under volume force. (first row) linear shape functions  $p=q=1$ , (second row) quadratic shape functions  $p=q=2$ , (from left to right)  $L^2$ -,  $H^1$ -, and energy-norm.

only very minor deviations compared to linear shape functions; first, the results for all coupling conditions coincide in each norm. Second, the convergence orders are 1.64 in the  $L^2$ -norm, 0.83 in the  $H^1$ -norm and 0.82 in the energy-norm, respectively. In conclusion, the optimal convergence orders are not obtained, the problem of order reduction is not cured at all by increasing the polynomial order of the shape functions.

The order reduction is caused by corner singularities at the clamped end of the square cantilever.



**Figure 20: Square cantilever under volume force.** Relative elementwise energy-error distribution on the macrodomain for (left)  $p=q=1$  and (right)  $p=q=2$ .

The relative elementwise error on the macrodomain is shown in Fig. 20. The error is computed by the ratio of the error in each element and the average energy per element. For the visualization of the error distribution the errors were calculated in the single elements of a coarse macro mesh. For both polynomial orders of shape functions the maximum absolute error is located in the corners of the cantilever's bearing. The high relative error of more than 50% for linear and more than 18% for quadratic shape functions indicates that the total energy in these elements is considerably higher than the average energy per element to which it is related here.

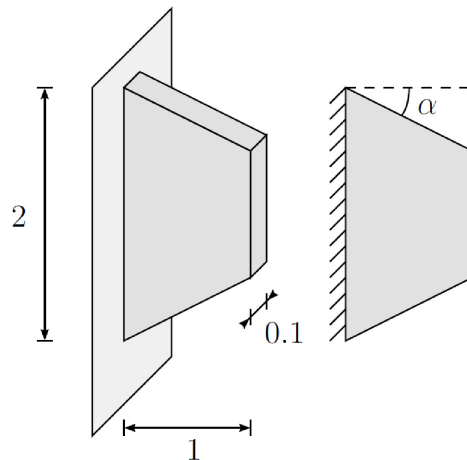


**Figure 21: Model of a tapered cantilever.**

**5.2.2 Tapered cantilever** If the angle  $\alpha$  is chosen sufficiently large ( $\alpha > 28.4^\circ$ ), then the design of a tapered cantilever as in Fig. 21 avoids the singularities of the square cantilever plate, which was proven by analytical means in Rössle [2000]. Here we choose

$\alpha = 30.4^\circ$ . Again, a volume load<sup>4</sup> of  $\mathbf{f} = [0, -10]^T [F/L^2]$  is applied to the cantilever and the sine wave-type microstructure with a Young's modulus contrast of 1.25 is chosen.

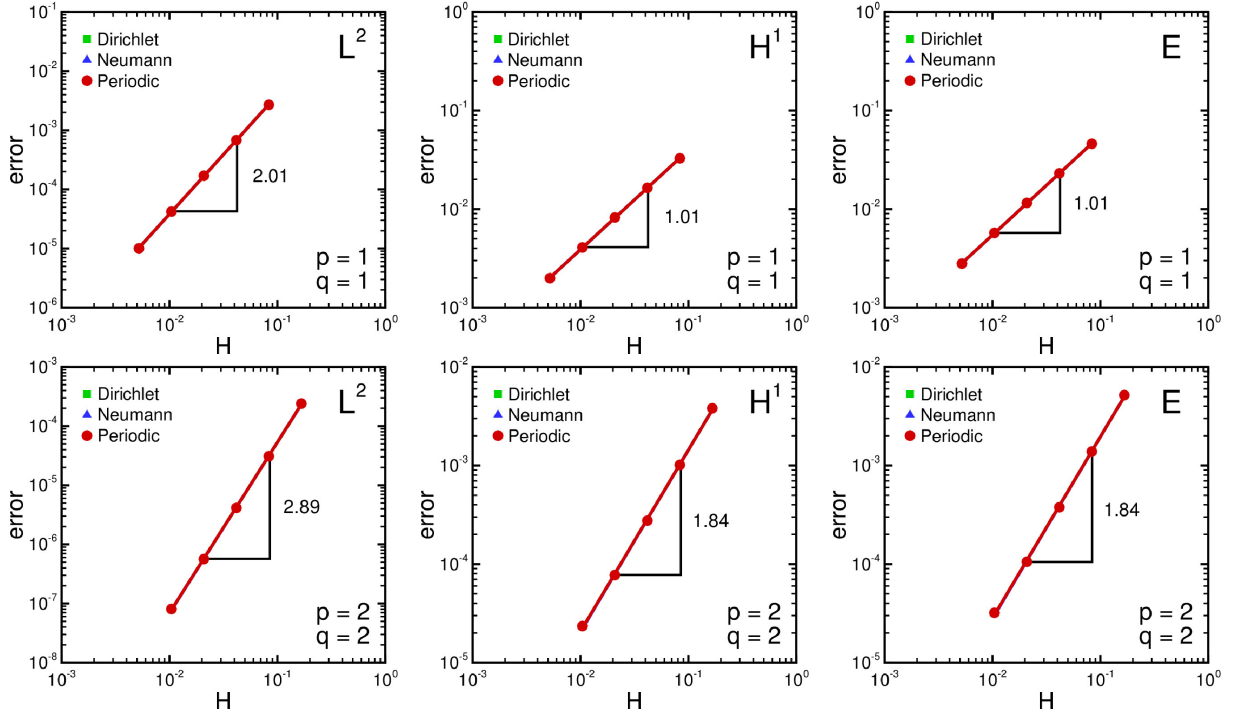


**Figure 22: Tapered cantilever under volume force.** Macroconvergence keeping the microdiscretization fixed, (first row) linear shape functions  $p=q=1$ , (second row) quadratic shape functions  $p=q=2$ , (from left to right)  $L^2$ -,  $H^1$ -, and energy-norm.

The convergence orders for linear shape functions are displayed in the diagrams of the first row in Fig. 22. In all norms the optimal convergence order is achieved. Again, the results of the different coupling conditions coincide.

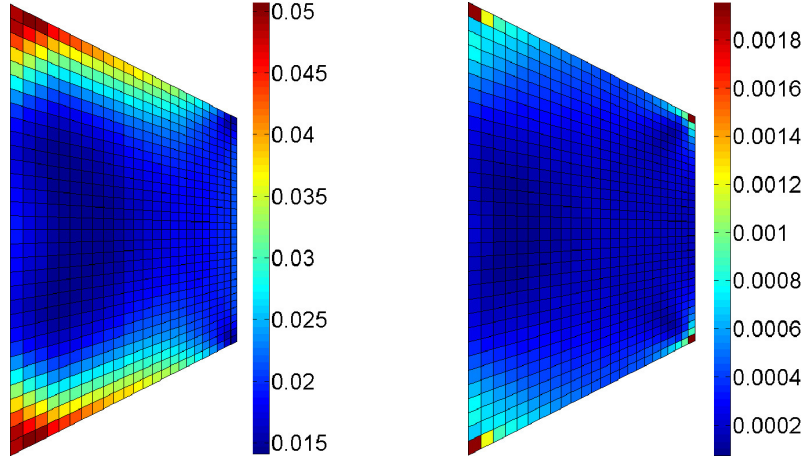
The results for quadratic shape functions in the second row of Fig. 22 exhibit minor deviations from the full, nominal convergence orders (2.89 instead of 3 in the  $L^2$ -norm, and 1.84 instead of 2 in the  $H^1$ - and energy-norm). However, compared to the considerable order reduction for the square plate, the present deviations are small.

Figure 23 displays the relative elementwise error distribution on the macrodomain of the tapered cantilever for linear and for quadratic shape functions. The relative error in the energy-norm is computed as in the previous example. The error distribution reveals that there is no longer a singularity in the lower and upper left corner due to the bearing of the plate. This leads to significantly lower relative errors in these areas.

### 5.3 Optimal uniform micro-macro refinement strategy

To investigate the optimal uniform micro-macro refinement strategy for linear and quadratic shape functions, the tapered cantilever is chosen as macro problem and the sine wave distribution is chosen as micro problem for their excellent regularity. The ratio of maximum to minimum Young's modulus is increased to 2.5.

<sup>4</sup>According to Rössle [2000] stress-free boundaries on  $\partial\mathcal{B}_N$  along with volume loads are an additional condition for the regularity of the BVP.



**Figure 23: Tapered cantilever under volume force.** Relative elementwise energy-error distribution on the macrodomain for (left)  $p=q=1$  and (right)  $p=q=2$ .

**5.3.1 Linear shape functions** For linear shape functions both on the micro and on the macro level the error in the  $L^2$ -norm is expected to converge in the order of  $p + 1 = 2$  on the macro and in the order of  $2q = 2$  on the micro level. Since micro and macro error converge in the same order, the micro mesh has to be refined in the same order as the macro mesh in order to achieve the optimal convergence order,  $N_{mic} = (N_{mac})^{p+1/2q} = N_{mac}$ .

The error in the  $H^1$ -/energy-norm converges in the order of  $p = 1$  on the macro level and in the order of  $2q = 2$  on the micro level. Here the micro error converges in a higher order which means that the micro mesh does not have to be refined "in the same order" as the macro mesh, see Jecker and Abdulle [2016] Tab. 1 on p.5 and in the present work Tab. 2,  $N_{mic} = (N_{mac})^{p/2q} = (N_{mac})^{1/2}$ .

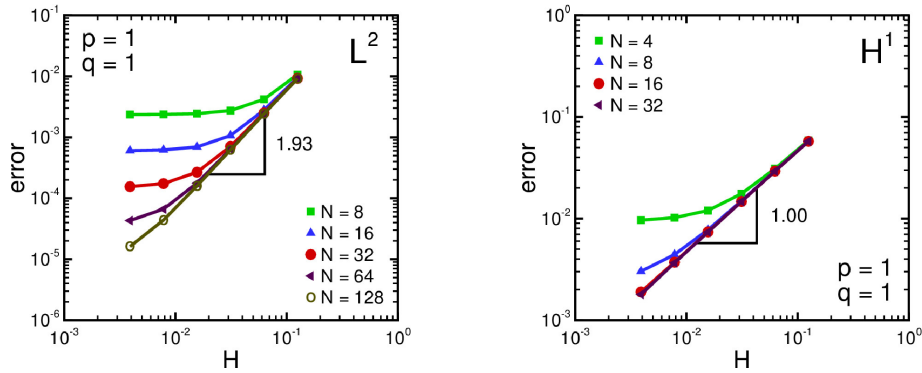


**Figure 24: Optimal uniform micro-macro refinement strategy.** (left) Error in the  $L^2$ -norm and (right) in the  $H^1$ -norm for linear shape functions,  $p=q=1$  with  $N = \epsilon/h$ .

Figure 24 shows the FE-HMM errors for different micro- and macrodiscretizations. For each line the microdiscretization is kept fixed where  $N$  is the number of elements per edge on the micro domain,  $N = \epsilon/h$ ; each marker in the diagrams denotes one macrodiscretization. If the micro mesh is not refined in the same order as the macro mesh, the error of the FE-HMM solution diverges from the line of optimal convergence in the  $L^2$ -norm. In the  $H^1$ -norm the micro mesh does not need not to be refined in the same order as the macro mesh so that the point where the single lines of fixed microdiscretizations diverge from the line of optimal convergence is shifted to finer macrodiscretizations.

**5.3.2 Quadratic shape functions** The use of quadratic shape functions leads to optimal convergence orders of  $p + 1 = 3$  on the macro level and  $2q = 4$  on the micro level in the  $L^2$ -norm,  $N_{mic} = (N_{mac})^{p+1/2q} = (N_{mac})^{3/4}$ . In the  $H^1$ -norm we have  $p = 2$  on the macro level and again  $2q = 4$  on the micro level,  $N_{mic} = (N_{mac})^{p/2q} = (N_{mac})^{1/2}$ .

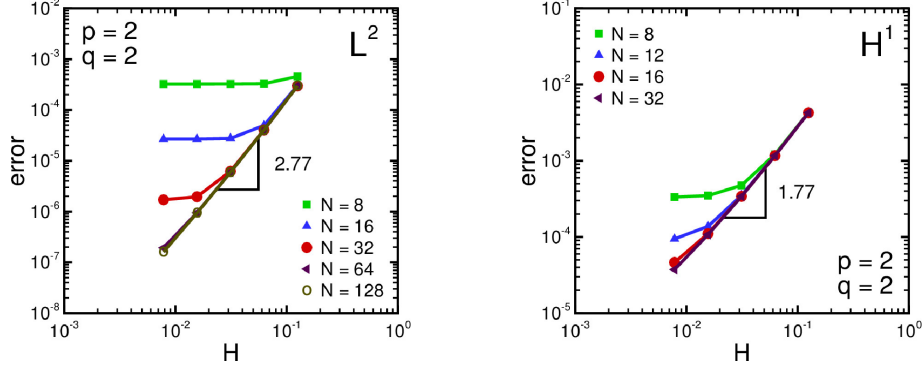


**Figure 25: Optimal micro macro refinement strategy.** Error in  $L^2$ -norm (left) and  $H^1$ -norm (right) with quadratic shape functions,  $p=q=2$  with  $N = \epsilon/h$ .

The results of the optimal refinement strategy analysis is shown in Fig. 25 for quadratic shape functions. Analogue to the linear case the micro mesh has to be refined in a reduced order for optimal convergence in the  $H^1$ -norm compared to the  $L^2$ -norm.

#### 5.4 Accuracy of error estimation

The accuracy of error estimation is compared with true error computation for the tapered cantilever subject to body forces along with a sine wave type Young's modulus distribution on the microscale and with PBC. Error estimation is based on the superconvergent patch recovery and on a simple averaging of elementwise stresses and strains. The results displayed in the diagrams of Fig. 26 indicate that the estimated errors are in good agreement with the calculated errors for both linear as well as quadratic shape functions.

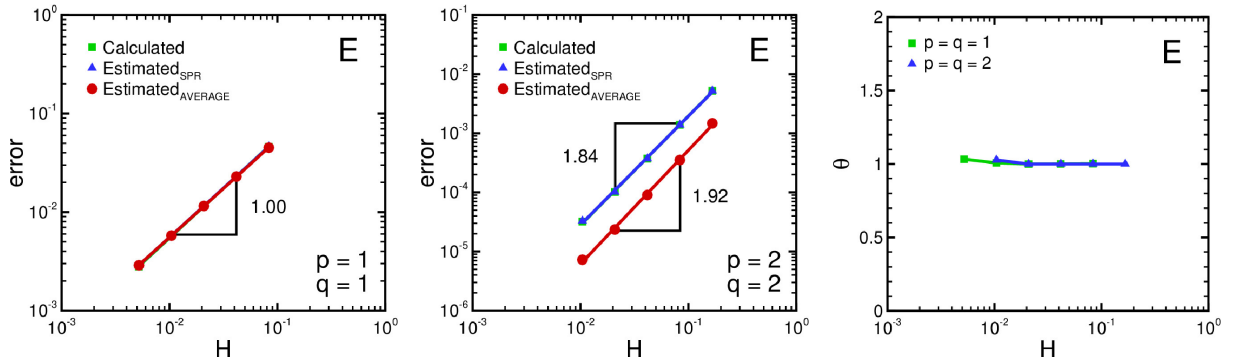


**Figure 26: Accuracy of macro error estimation.** Calculated and estimated error in the energy-norm for (left)  $p=q=1$ , for (center)  $p=q=2$ , and (right) the corresponding effectivity index  $\theta$ .

Notice that if the error estimator is restricted to the macro error part, the computation of the true total error along the lines of an optimal uniform micro-macro refinement strategy as verified in Sec.5.3 cannot be replaced by suchlike error estimation.

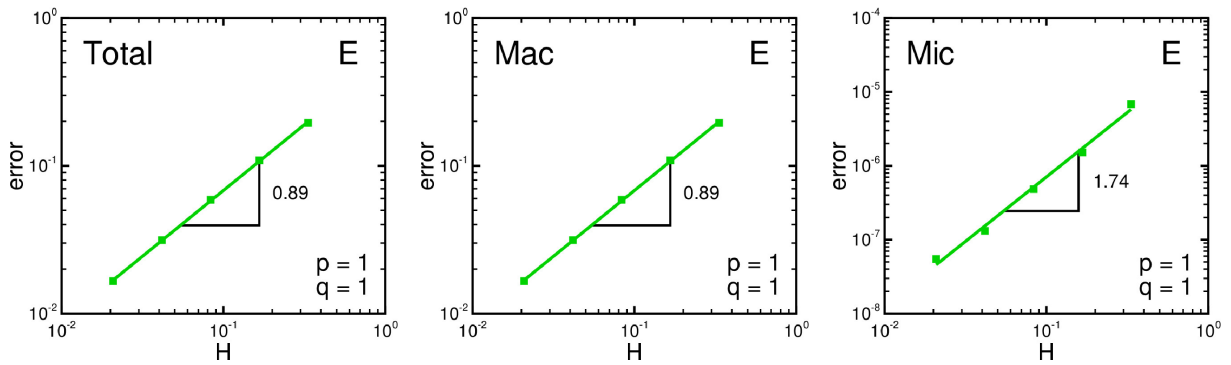
We mention in passing that in the present example for the considered discretizations

the macro error is orders of magnitude larger than the micro error, a result that will be quantitatively analyzed for the example in the consecutive Subsec. 5.5

### 5.5 Efficient decomposition of the true errors

The efficient decomposition of the computed error into its macro and micro parts according to Tab. 3 in Subsec. 4.2 shall be demonstrated for the tapered beam with the sine wave type Young's modulus distribution along with PBC. Here, in contrast to Sec. 5.4, a line load is applied to the free end of structure.

Steps 1.) and 2.) in Tab. 3 are carried out along with the corresponding reference solutions ( $H \rightarrow 0$  by  $1536 \times 2048$  elements, and  $h \rightarrow 0$  by  $1024 \times 1024$  elements). The microscopic error then directly follows as the difference between total error and macroscopic error.



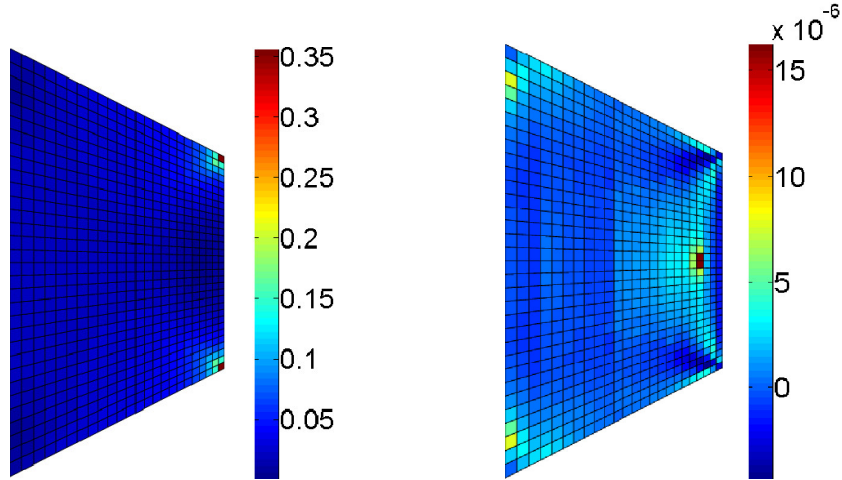
**Figure 27: Tapered cantilever under line load.** Total error (left), macroscopic error (center) and microscopic error (right).

Figure 27 shows the magnitude and convergence of the three different errors. The considerably larger values of the macro error compared to the micro error indicate the stronger influence of the macro discretization on the accuracy compared with the influence of the micro discretization. As a consequence, the total error and the macroscopic error are close together. The convergence rates are somewhat below the theoretical values which is true for each of the three errors.

Figure 28 displays the distributions of the total error and the micro error. Recall that suchlike error decomposition clearly cannot be carried out by the error estimator operating on the macroscale, compare Remark 2 in Sec. 4.3.2.

### 5.6 Modeling error

Next, the modeling error for Dirichlet coupling along with a noninteger ratio  $\delta/\epsilon$  is examined, cf. (42)–(44) along with (45). In the analysis the macro problem of the square plate under volume forces is used, the micro problem is the sine wave stiffness distribution. In order to investigate the convergence and show the modeling error, the macro discretization is continuously refined, while a very fine micro discretization ensures negligible micro errors. The calculations are run with  $\delta/\epsilon = 1$  for PBC to indicate the optimal convergence of the macro problem without any modeling error. For Dirichlet coupling the cases  $\delta/\epsilon \in \{1.0, 1.1, 5/3, 2.0\}$  are considered somewhat increasing the range of  $\delta/\epsilon$  in Jecker



**Figure 28: Tapered cantilever under line load.** Relative elementwise energy-error distribution on the macrodomain for  $p=q=1$  with (left) the total discretization error and (right) the micro error.

and Abdulle [2016]. The reference solution for error calculation is obtained for PBC and a very fine macro mesh.

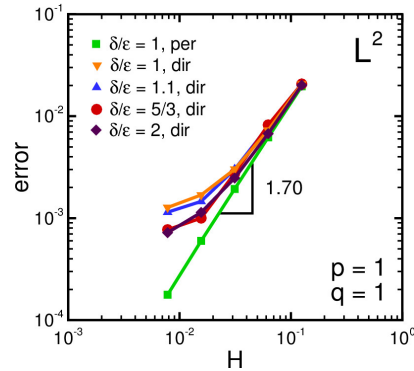


**Figure 29: Error convergence for different ratios of  $\delta/\epsilon$ .** Calculated errors for periodic coupling with  $\delta/\epsilon = 1$  and for Dirichlet coupling with  $\delta/\epsilon \in \{1.0, 1.1, 5/3, 2.0\}$ ,  $\epsilon = 0.005$ .

Figure 29 depicts the results of the error calculations. For  $\delta/\epsilon = 1$  and PBC the expected constant order is observed; it is the case already reported in Fig. 19 for  $p=q=1$  showing a somewhat reduced convergence order of 1.70. In contrast to the constant convergence for the reference case of  $\delta/\epsilon = 1$  along with PBC the case of Dirichlet coupling along with various  $\delta/\epsilon$  ratios exhibit an offset between the corresponding curves and the reference solution. This offset indicates the modeling error, which becomes increasingly dominant compared to the macro error for macro mesh refinement. Notice that the modeling error increases for an increasing ratio  $\epsilon/\delta$  for  $\delta > \epsilon$  in agreement with (45).

## 6 Summary and conclusions

The aim of the present work was the numerical analysis of energetically consistent micro-coupling conditions in the homogenization framework of a two-scale finite element method. The obtained results are valid for FE-HMM and FE<sup>2</sup> for the coincidence of the methods,

which was shown in Eidel and Fischer [2018]. The main results shall be summarized.

1. The **micro error convergence analysis** for different micro problems, micro-macro coupling conditions and polynomial orders of shape functions has led to the following results.
  - (a) We have clarified the distinction between the micro-error measured on the microscale with the theoretical convergence order of  $q+1$  and  $q$  in the  $L^2$ -norm and the  $H^1$ -/energy-norm, respectively, and the micro error as propagated to the macroscale with the -somewhat surprising- convergence order of  $2q$  in all ( $L^2$ -,  $H^1$ -, energy-) norms.
  - (b) For sufficiently regular micro problems the a priori error estimates of FE-HMM have been confirmed for each of the considered ( $L^2$ -,  $H^1$ -, energy-) norms. The micro-coupling conditions show no significant deviation from each other in the measured convergence order.
  - (c) The regularity of a micro BVP requires a microstructure with smooth distribution of the heterogeneous material parameters (here: Young's modulus). Then the contrast of maximum to minimum material parameters does not influence the convergence order. Vice versa, a stiffness-jump at interfaces in the RVE lowers the convergence order for linear shape functions, and quadratic shape functions do not cure the order reduction.
2. The **constant traction (Neumann) condition**
  - (a) Two methods for Neumann conditions have been compared, the recently introduced semi-Dirichlet ansatz Javili et al. [2017] with the mass-type perturbation technique for regularization Miehe and Koch [2002]. The two methods coincide in the goal but differ in the methodic procedure to remove rigid body motions from the RVE and the corresponding singularity of the stiffness matrix.
  - (b) Both methods are accurate in fulfilling the condition of constant traction. The approach of Miehe & Koch turns out to be remarkably insensitive to the particular choice of the perturbation parameter in a wide parameter range. It is most simple to implement and fast. The Semi-Dirichlet ansatz carries out explicit static condensation of rigid body motions by additional Dirichlet conditions of the RVE. Since this approach requires an iterative solution, it is more expensive than the perturbation technique.
3. The **macro error convergence analysis** for two different macro problems applying different micro-macro coupling conditions and linear as well as quadratic shape functions has led to the following results.
  - (a) For fully regular macro BVPs the error estimates have been confirmed in all norms. Singularities spoil the convergence such that the order is below the theoretical estimate for linear shape functions, which implies no improvement in the order for quadratic shape functions.
  - (b) Two macroproblems underpin the aforementioned statements; a square cantilever which does not achieve the full order due to singularities in the corners of the bearing. At these points and their direct neighborhood the error are

maximal. A tapered cantilever plate avoids by its geometry these singularities and enables therefore full order in agreement with the a priori error estimates, which is true for linear shape functions and for quadratic shape functions along with only minor deviations.

- (c) The choice of the coupling conditions on the RVE does not affect the macro convergence order nor the quantitative macro error.

#### 4. Error estimation and optimal mesh refinements

The recovery-type, superconvergent error estimator of Zienkiewicz and Zhu [1992a] was implemented on the macroscale; it exhibits the following properties:

- (a) The error estimator is accurate as indicated by an efficiency index close to unity; the estimated error almost equals the computed discretization error.
- (b) The optimal uniform micro-macro refinement strategies directly following from the a priori error estimates were confirmed for linear and quadratic shape functions. These refinement strategies are of considerable practical value since they enable the optimal convergence of the total error while keeping the numerical effort minimal.
- (c) Although the error estimator on the macroscale exhibits different estimates at (macro-, micro-) discretizations  $(H, h)$  and  $(H, h/2)$ , it merely measures macro discretization errors. The difference in the error estimations for various  $h$  is on the macroscale not a discretization error but a modeling error, since indeed the same type of constitutive law is used on the microscale but for different material parameters, which depend on the microdiscretization  $h$ .

- 5. **Analysis of the modeling error.** The modeling error for Dirichlet coupling along with various  $\delta/\epsilon$  ratios was identified and made measurable by uniform macro mesh refinements along with fine micro meshes. The simulation results underpin the a priori estimate in that the modeling error increases for an increasing  $\epsilon/\delta$  ratio with  $\delta > \epsilon$ . Moreover, for  $H \rightarrow 0$  and  $h \rightarrow 0$  the modeling error persists as a discretization-independent residual, again consistent with the estimate.

**Acknowledgements.** Bernhard Eidel acknowledges support by the Deutsche Forschungsgemeinschaft (DFG) within the Heisenberg program (grant no. EI 453/2-1). Simulations were performed with computing resources granted by RWTH Aachen University under project ID prep0005.

**Declaration of Interest.** None.

## A Appendix

### A.1 Derivation of the micro-to-macro stiffness transformation matrix

The derivation of the macro element stiffness matrix part  $\mathbf{k}_{IJ}^{e,mac}$  in (16) shall be detailed:

$$\begin{aligned}
\mathbf{k}_{IJ}^{e,mac} &= B_H^e [\mathbf{N}_I^H, \mathbf{N}_J^H] \\
&= \sum_{l=1}^{N_{qp}} \frac{\omega_{K_l}}{|K_\delta|} \int_{K_\delta} \left( \mathbf{L} \mathbf{u}_{K_\delta}^{h(I,x_i)} \right)^T \mathbb{A}^\epsilon \mathbf{L} \mathbf{u}_{K_\delta}^{h(J,x_i)} dV \\
&= \sum_{l=1}^{N_{qp}} \frac{\omega_{K_l}}{|K_\delta|} \int_{K_\delta} \left( \mathbf{L} \sum_{m=1}^{M_{mic}} \mathbf{N}_{m,K_\delta}^h \mathbf{d}_m^{h(I,x_i)} \right)^T \mathbb{A}^\epsilon \mathbf{L} \sum_{n=1}^{M_{mic}} \mathbf{N}_{n,K_\delta}^h \mathbf{d}_n^{h(J,x_i)} dV \\
&= \sum_{l=1}^{N_{qp}} \frac{\omega_{K_l}}{|K_\delta|} \sum_{T \in \mathcal{T}_h} \int_T \left( \mathbf{L} \sum_{m=1}^{n_{node}} \mathbf{N}_{m,K_\delta}^h \mathbf{d}_m^{h(I,x_i)} \right)^T \mathbb{A}^\epsilon \mathbf{L} \sum_{n=1}^{n_{node}} \mathbf{N}_{n,K_\delta}^h \mathbf{d}_n^{h(J,x_i)} dV \\
&= \sum_{l=1}^{N_{qp}} \frac{\omega_{K_l}}{|K_\delta|} \sum_{T \in \mathcal{T}_h} \int_T \left( \mathbf{L} \sum_{m=1}^{n_{node}} \mathbf{N}_{m,K_\delta}^h \mathbf{d}_m^{h(I,x_i)} \right)^T \mathbb{A}^\epsilon \mathbf{L} \sum_{n=1}^{n_{node}} \mathbf{N}_{n,K_\delta}^h \mathbf{d}_n^{h(J,x_i)} dV \\
&= \sum_{l=1}^{N_{qp}} \frac{\omega_{K_l}}{|K_\delta|} \left( \mathbf{d}^{h(I,x_i)} \right)^T \sum_{T \in \mathcal{T}_h} \int_T \sum_{m=1}^{n_{node}} \sum_{n=1}^{n_{node}} \left( \mathbf{L} \mathbf{N}_{m,K_\delta}^h \right)^T \mathbb{A}^\epsilon \mathbf{L} \mathbf{N}_{n,K_\delta}^h dV \mathbf{d}_n^{h(J,x_i)} \\
&= \sum_{l=1}^{N_{qp}} \frac{\omega_{K_l}}{|K_\delta|} \left( \mathbf{d}^{h(I,x_i)} \right)^T \sum_{T \in \mathcal{T}_h} \left( \sum_{m=1}^{n_{node}} \sum_{n=1}^{n_{node}} \int_T \mathbf{B}_m^{e,T} \mathbb{A}^\epsilon \mathbf{B}_n^e dV \mathbf{d}_n^{h(J,x_i)} \right) \quad (\text{A.1}) \\
&= \sum_{l=1}^{N_{qp}} \frac{\omega_{K_l}}{|K_\delta|} \sum_{T \in \mathcal{T}_h} \left( \sum_{m=1}^{n_{node}} \sum_{n=1}^{n_{node}} \left( \mathbf{d}_m^{h(I,x_i)} \right)^T \mathbf{k}_{mn}^{e,mic} \mathbf{d}_n^{h(J,x_i)} \right) \\
&= \sum_{l=1}^{N_{qp}} \frac{\omega_{K_l}}{|K_\delta|} \left( \mathbf{d}^{h(I)} \right)^T \sum_{T \in \mathcal{T}_h} \mathbf{k}_{K_\delta}^{e,mic} \mathbf{d}^{h(J)} \\
&= \sum_{l=1}^{N_{qp}} \frac{\omega_{K_l}}{|K_\delta|} \left( \mathbf{d}^{h(I)} \right)^T \mathbf{K}_{K_\delta}^{mic} \mathbf{d}^{h(J)},
\end{aligned}$$

where  $\mathbf{d}^{h(I)} = \left( \mathbf{d}^{h(I,x_1)} | \mathbf{d}^{h(I,x_2)} | \mathbf{d}^{h(I,x_3)} \right)$  for  $n_{dim} = 3$ . The assembly of  $\mathbf{k}_{IJ}^{e,mac}$  results in

$$\mathbf{k}_K^{e,mac} = \sum_{l=1}^{N_{qp}} \frac{\omega_{K_l}}{|K_l|} \mathbf{T}_{K_l}^T \mathbf{K}_{K_l}^{mic} \mathbf{T}_{K_l} \quad (\text{A.2})$$

$$\text{with } \mathbf{T}_{K_l} = \left[ \left[ \mathbf{d}^{h(I,x_i)} \right]_{i=1,\dots,n_{dim}} \right]_{I=1,\dots,N_{node}}. \quad (\text{A.3})$$

## A.2 Definition of norms

The norms used in the present work are defined according to

$$L^2\text{-norm: } \|\mathbf{u}\|_{L^2(\Omega)} := \sqrt{\int_{\Omega} \mathbf{u} : \mathbf{u} \, dV}, \quad (\text{A.4})$$

$$H^1\text{-norm: } \|\mathbf{u}\|_{H^1(\Omega)} := \sqrt{\left( \sum_{i,j=1}^d \int_{\Omega} \left( \frac{\partial u_i}{\partial x_j} \right)^2 \, dV + \sum_{i=1}^d \int_{\Omega} (u_i)^2 \, dV \right)}, \quad (\text{A.5})$$

$$\text{energy-norm: } \|\mathbf{u}\|_{A(\Omega)} := \sqrt{\int_{\Omega} \mathbb{A} \boldsymbol{\varepsilon}(\mathbf{u}) : \boldsymbol{\varepsilon}(\mathbf{u}) \, dV} = \sqrt{\mathbf{d}^T \mathbf{K} \mathbf{d}}. \quad (\text{A.6})$$

## A.3 Direct implementation of Dirichlet and periodic coupling conditions

When Dirichlet or periodic boundary conditions are implemented in a direct manner without using Lagrange multipliers the micro system of equations reads as

$$\mathbf{K}_{K_l}^{mic} \mathbf{d}^{h(I,x_i)} = \mathbf{0} \quad (\text{A.7})$$

for a macroscopic unit displacement state  $(I, x_i)$ , a notation that is dropped in the following for notational convenience along with the subscript  $K_l$  indicating quadrature point  $l$  of macro element  $K$ .

For Dirichlet coupling conditions the micro displacements  $\mathbf{d}^h$  are known since they directly follow from the macroscopic displacement field. For that reason we decompose the microscopic displacement vector

$$\mathbf{d}^h = [\mathbf{d}_D^h, \mathbf{d}_F^h]^T \quad (\text{A.8})$$

into the known displacements  $\mathbf{d}_D^h$  and an unknown part  $\mathbf{d}_F^h$ . Then the system of equations follows the form

$$\begin{bmatrix} \mathbf{K}_{DD}^{mic} & \mathbf{K}_{FD}^{mic} \\ \mathbf{K}_{DF}^{mic} & \mathbf{K}_{FF}^{mic} \end{bmatrix} \begin{bmatrix} \mathbf{d}_D^h \\ \mathbf{d}_F^h \end{bmatrix} = \begin{bmatrix} \mathbf{0} \\ \mathbf{0} \end{bmatrix}. \quad (\text{A.9})$$

It follows that

$$\mathbf{K}_{DF}^{mic} \mathbf{d}_D^h + \mathbf{K}_{FF}^{mic} \mathbf{d}_F^h = \mathbf{0} \quad (\text{A.10})$$

which yields the unknown micro displacements according to

$$\mathbf{d}_F^h = -(\mathbf{K}_{FF}^{mic})^{-1} (\mathbf{K}_{FD}^{mic} \mathbf{d}_D^h). \quad (\text{A.11})$$

For periodic coupling conditions the direct implementation accounts for the fact that not the micro displacements but the fluctuations between macroscopic and microscopic displacement fields are periodic on opposite boundaries.

First we introduce the fluctuations on the microlevel as the difference between macroscopic and microscopic displacements

$$\tilde{\mathbf{d}}^h = \mathbf{d}^H - \mathbf{d}^h . \quad (\text{A.12})$$

Since the system of equations from (A.7) only contains the microscopic displacements, we decompose them into the homogeneous deformation part following from the macroscopic displacements  $\mathbf{d}^H$  and their fluctuations  $\tilde{\mathbf{d}}^h$

$$\mathbf{d}^h = \mathbf{d}^H + \tilde{\mathbf{d}}^h , \quad (\text{A.13})$$

which is inserted into (A.7) and yields the solution

$$\tilde{\mathbf{d}}^h = (\mathbf{K}^{mic})^{-1} (-\mathbf{K}^{mic} \mathbf{d}^H) . \quad (\text{A.14})$$

Equation (A.14) is solved accounting for periodic boundaries. Rigid body motions are removed from the system simply by fixing one arbitrary node in each direction of space. A convenient choice for periodic structures is to set the displacements of a node in the center of an RVE to zero.

## References

- A. Abdulle, On a-priori error analysis of fully discrete Heterogeneous Multiscale FEM, *SIAM Multiscale Model. Simul.* 4,2 (2005) 447–459.
- A. Abdulle, Analysis of the heterogeneous multiscale FEM for problems in elasticity, *Math. Models Methods Appl. Sci.* 16(4) (2006) 615–635.
- A. Abdulle, The Finite Element Heterogeneous Multiscale Method: a computational strategy for multiscale PDEs, *Math. Sci. Appl.*, Vol. 31 31 (2009) 133–181.
- A. Abdulle, A. Nonnenmacher, Adaptive finite element heterogeneous multiscale method for homogenization problems, *Comput. Methods Appl. Mech. Engrg.* 200 (2011) 2710–2726.
- A. Abdulle, A. Nonnenmacher, A posteriori error estimates in quantities of interest for the finite element heterogeneous multiscale method, *Numer. Meth. Part. D. E.* 29(5) (2013) 1629–1656.
- A. Abdulle, C. Schwab, Heterogeneous multiscale FEM for diffusion problems on rough surfaces, *Multiscale Model. Simul.* 3(1) (2005) 195–220.
- A. Abdulle, W. E., B. Engquist, E. Vanden-Eijnden, The heterogeneous multiscale method, *Acta Numer.* 466 (2012) 1–87.
- G. Allaire, Homogenization and two-scale convergence. *SIAM J. Math. Anal.* 23 (1992) 1482–1518.
- J. Barlow, Optimal stress locations in finite element models, *Int. J. Numer. Methods Eng.* 10 (1976) 243–251.

- A. Bensoussan, J.L. Lions, G. Papanicolau, *Asymptotic Analysis for Periodic Structures*, North-Holland, Amsterdam (1976).
- D. Cioranescu, P. Donato, *An Introduction to Homogenization*, Oxford University Press, New York (1999).
- M. Döskár, J. Zeman, D. Jarůšková, J. Novák, Wang tiling aided statistical determination of the Representative Volume Element size of random heterogeneous materials. *Eur. J. Mech. A-Solid* 70 (2018) 280–295.
- H.L. Duan, J. Wang, Z.P. Huang, and B.L. Karihaloo, Size-dependent effective elastic constants of solids containing nano-inhomogeneities with interface stress. *J. Mech. Phys. Solids* 53(7) (2005) 1574–1596.
- W. E, B. Engquist, The heterogeneous multi-scale methods, *Commun. Math. Sci.* 1 (2003) 87–132.
- W. E, B. Engquist, Z. Huang, Heterogeneous multiscale method: A general methodology for multiscale modeling, *Phys. Rev. B: Condens. Matter* 67 (2003) 092101.
- W. E, B. Engquist, X. Li, W. Ren, E. Vanden-Eijnden, Heterogeneous Multiscale Methods: A Review, *Commun. Comput. Phys* 2 (2007) 367–450.
- W. E, P. Ming, P. Zhang, Analysis of the heterogeneous multi-scale method for elliptic homogenization problems, *J. Amer. Math. Soc.* 18 (2005) 121–156.
- B. Eidel, A. Fischer, The heterogeneous multiscale finite element method FE-HMM for the homogenization of linear elastic solids, *PAMM* 16 (2016) 521–522.
- B. Eidel, A. Fischer, The heterogeneous multiscale finite element method FE-HMM for the homogenization of linear elastic solids, *Comput. Methods Appl. Mech. Engrg.* 329 (2018) 332–368.
- C.A. Felippa, K.C. Park, The construction of free-free flexibility matrices for multilevel structural analysis, *Comput. Methods Appl. Mech. Engrg.* 191 (2002) 2139–2168.
- F. Feyel, J.L. Chaboche, FE<sup>2</sup> multiscale approach for modelling the elastoviscoplastic behaviour of long fibre SiC/Ti composite materials, *Comput. Methods Appl. Mech. Engrg.* 183 (2000) 309–330.
- J. Fish, Q. Yu, K. Shek, Computational damage mechanics for composite materials based on mathematical homogenization, *Int. J. Numer. Meth. Eng.* 45 (1999) 1657–1679.
- M.G.D. Geers, V.G. Kouznetsova, W.A.M. Brekelmans, Multi-scale computational homogenization: trends and challenges, *J. Comput. Appl. Math.* 234 (2010) 2175–2182.
- M.G.D. Geers, V.G. Kouznetsova, W.A.M. Brekelmans, Computational homogenization, in: R. Pippan, P. Gumbsch (Eds.), *Multiscale Modelling of Plasticity and Fracture by Means of Dislocation Mechanics*, CISM International Centre for Mechanical Sciences, (2010) 327–394.

- 
- S. Hazanov, C. Huet, Order relationships for boundary conditions effect in heterogeneous bodies smaller than the representative volume, *J. Mech. Phys. Solids* 42(12) (1994) 1995–2011.
- R. Hill, Elastic properties of reinforced solids: some theoretical principles, *J. Mech. Phys. Solids* 11 (1963) 357–372.
- R. Hill, On constitutive macro-variables for heterogeneous solids at finite strain, *Proc. R. Soc. London, Ser. A* 326 (1972) 131–147.
- T.J.R. Hughes, *The finite element method: linear static and dynamic finite element analysis*, Dover Publications, Mineola, New York (2000).
- A. Javili, S. Saeb, P. Steinmann, Aspects of implementing constant traction boundary conditions in computational homogenization via semi-Dirichlet boundary conditions *Comput. Mech.* 59 (2017) 21–35.
- O. Jecker, A. Abdulle, Numerical experiments for multiscale problems in linear elasticity, in: B. Karasözen, M. Manguoğlu M., M. Tezer-Sezgin, S. Göktepe, Ö. Uğur (Eds.) *Numerical Mathematics and Advanced Applications ENUMATH 2015. Lecture Notes in Computational Science and Engineering*, vol. 112. Springer, Cham (2016) 123–131.
- T. Kanit, S. Forest, I. Galliet, V. Mounoury, D. Jeulin, Determination of the size of the representative volume element for random composites: statistical and numerical approach, *Int. J. Solids Struct.* 40(13–14) (2003) 3647–3670.
- V. Kouznetsova, W.A.M. Brekelmans, F.P.T. Baaijens, An approach to micro-macro modeling of heterogeneous materials, *Comput. Mech.* 27 (2002) 37–48.
- V. Kouznetsova, M.G.D. Geers, W.A.M. Brekelmans, Multi-scale constitutive modelling of heterogeneous materials with a gradient-enhanced computational homogenization scheme, *Int. J. Numer. Meth. Eng.* 54 (2002) 1235–1260.
- F. Larsson, K. Runesson, S. Saroukhani, R. Vafadari, Computational homogenization based on a weak format of micro-periodicity for RVE-problems, *Comput. Methods Appl. Mech. Engrg.* 1-4 (2011) 11–26.
- J.C. Michel, H. Moulinec, P. Suquet, Effective properties of composite materials with periodic microstructure: a computational approach, *Comput. Methods Appl. Mech. Engrg.* 172 (1999) 109–143.
- C. Miehe, J. Schröder, J. Schotte, Computational homogenization analysis in finite plasticity Simulation of texture development in polycrystalline materials, *Comput. Methods Appl. Mech. Engrg.* 171 (1999) 387–418.
- C. Miehe, J. Schotte, J. Schröder, Computational homogenization analysis in finite plasticity Simulation of texture development in polycrystalline materials, *Comput. Mat. Sci.* 16 (1-4) (1999) 372–382.
- C. Miehe, A. Koch, Computational micro-to-macro transitions of discretized microstructures undergoing small strain, *Arch. Appl. Mech.* 71 (2002) 300–317.

- C. Miehe, Computational micro-to-macro transitions for discretized micro-structures of heterogeneous materials at finite strains based on the minimization of averaged incremental energy, *Comput. Methods Appl. Mech. Engrg.* 192 (2003) 559–591.
- M. Ohlberger, A posteriori error estimates for the heterogeneous multiscale finite element method for elliptic homogenization problems, *Multiscale Model. Simul.* 4(1) (2005) 88–114.
- M. Ostoja-Starzewski, Material spatial randomness: from statistical to representative volume element. *Probabilist. Eng. Mech.* 21(2), 112–132.
- D. Perić, E.A. de Souza Neto, R.A. Feijóo, M. Partovi, A.J. Carneiro Molina, On micro-to-macro transitions for multi-scale analysis of non-linear heterogeneous materials: unified variational basis and finite element implementation. *Int. J. Numer. Methods Eng.* 87 (2010) 149–170.
- K. Pham, V.G. Kouznetsova, M.G.D. Geers, Transient computational homogenization for heterogeneous materials under dynamic excitation, *J. Mech. Phys. Solids* 61 (2013) 2125–2146.
- A. Rössle, Corner Singularities and Regularity of Weak Solutions for the Two-Dimensional Lam Equations on Domains with Angular Corners, *J. Elast.* 60 (2000) 57–75.
- S. Saeb, P. Steinmann, A. Javili, Aspects of computational homogenization at finite deformations: a unifying review from Reuss’ to Voigt’s bound, *Appl. Mech. Rev.* 68 (2016) 050801.
- E. Sanchez-Palencia, *Non-Homogeneous Media and Vibration Theory*, Lecture Notes in Physics, Vol. 127, Springer, Berlin (1980).
- J. Schröder, A numerical two-scale homogenization scheme: the FE<sup>2</sup>-method, in: J. Schröder, K. Hackl (Eds.), *Plasticity and Beyond*, CISM International Centre for Mechanical Sciences, (2014) 1–64.
- A. Sridhar, V.G. Kouznetsova, M.G.D. Geers, A general multiscale framework for the emergent effective elastodynamics of metamaterials, *J. Mech. Phys. Solids* 111 (2018) 414–433.
- P. Suquet, *Elements of Homogenization for Inelastic Solid Mechanics*, in: E. Sanchez-Palencia, A. Zaoui (Eds.), *Homogenization Techniques for Composite Media*, Springer-Verlag, Berlin (1987) 193–287.
- X.-Y. Yue, W. E, The local microscale problem in the multiscale modelling of strongly heterogeneous media: Effect of boundary conditions and cell size, *J. Comput. Phys.* 222 (2007) 556–572.
- O.C. Zienkiewicz, J.Z. Zhu, The superconvergent patch recovery and a posteriori error estimates. part 1: the recovery technique, *Int. J. Numer. Methods Eng.* 33 (1992) 1331–1364.
- O.C. Zienkiewicz, J.Z. Zhu, The superconvergent patch recovery and a posteriori error estimates. part 2: error estimates and adaptivity, *Int. J. Numer. Methods Eng.* 33 (1992) 1365–1382.